ADVANCED CONSIDERATIONS IN LIDAR TECHNOLOGY: APPLICATION
ENHANCEMENT, INSPECTION WORKFLOW IMPLEMENTATION AND DATA
COLLECTION QUALITY MANAGEMENT

by

Haitao Bian

A dissertation submitted to the faculty of
The University of North Carolina at Charlotte
in partial fulfillment of the requirements
for the degree of Doctor of Philosophy in
Infrastructure and Environmental Systems

Charlotte

2012

Approved by:

_____
Dr. Shen-En Chen

_____
Dr. Edd Hauser

_____
Dr. Martin Kane

_____
Dr. Yesim Sireli

_____
Dr. Don Chen

ABSTRACT

HAITAO BIAN. Advanced considerations in LiDAR technology: application enhancement, inspection workflow implementation and data collection quality management. (Under the direction of DR. SHEN-EN CHEN)

Bridge inspection is a critical topic in infrastructure management and is facing unprecedented challenges as the public is concerned more about bridge safety after a series of bridge failures. LiDAR based remote sensing is recommended as a way in supplementing the prevailing visual inspection to quantify critical bridge information. In this research, focus will be placed on the advanced considerations of LiDAR technology in bridge inspection, including the application evaluation, inspection workflow implementation, and data collection quality management. Particularly, efforts on improving the computational performance of the original damage detection algorithm have been carried out and the use of reflectivity data is introduced as a new feature to enhance the algorithm's capability in defect recognition. The specific applications that using LiDAR technology to evaluate bridge deck joint and monitoring simulated slope erosion have been studied. This research further studied the inspection workflow implementation and the sources of errors in the LiDAR bridge inspection. Quality management has also been considered to improve the bridge inspection data quality besides the development of advanced inspection technology. In the end, comparative cost analysis is conducted to determine the savings for implementing LiDAR technology into bridge inspection workflow.

ACKNOWLEDGMENTS

TABLE OF CONTENTS

LIST OF TABLES

LIST OF FIGURES

LIST OF ABBREVIATIONS

AASHTO	American Association of State Highway and Transportation Officials
ASCE	American Society of Civil Engineering
AW	Annual Worth
BJA	Bridge Joint Association
BMS	Bridge Management System
CBA	Cost Benefit Analysis
CRS	Commercial Remote Sensing
DOT	Department of Transportation
EMA	Experimental Modal Analysis
FBG	Fiber Bragg-Grating
FFT	Fast Fourier Transform
FHT	Fast Haar Transform
FHWA	Federal Highway Administration
FRP	Fiber-Reinforce Polymer
GIS	Geographic Information System
GPS	Global Position System
IRSV	Integrated Remote Sensing and Visualization
LiBE	LiDAR based Bridge Evaluation
LiDAR	Light Ranging and Detection
MSE	Mean Square Error
NBIS	National Bridge Inspection Standards
NHI	National Highway Institute

PV   Present Value

QC/QA   Quality Control and Quality Assurance

RITA   Research Innovative Technology Administration

SI   Spatial Information

SISFAP   Spatially-Integrated Small Format Aerial Photography

USDOT   U.S. Department of Transportation

CHAPTER 1: INTRODUCTION

1.1 Bridge Failures and Maintenance

Since the 1960s, bridge safety has been recognized as a national interest after a series of bridge failures in the United States. The collapse of the Silver Bridge at Point Pleasant, West Virginia, in 1967 resulted in 46 deaths and the establishment of the national bridge inspection program (Brinckerhoff, 1993). The I35 bridge collapse at Minneapolis, Minnesota, in 2007 further challenged current bridge safety monitoring program (Subramanian, 2008). There is an alarming increase in bridge failures in the USA (Imhof, 2005 and McLinn, 2009). Figure 1.1 shows the U.S. bridge failure data since the middle of 19th century to current.
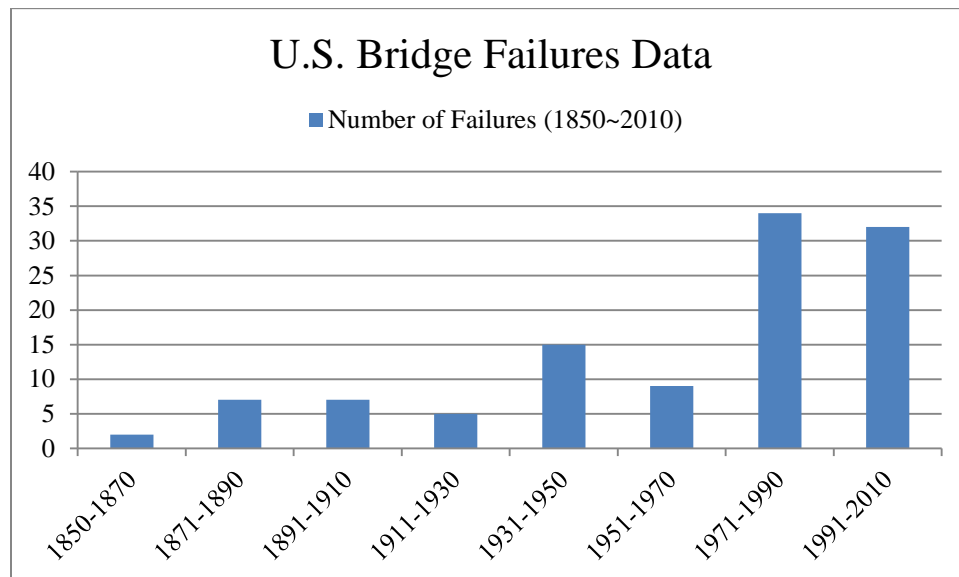
Figure 1.1 U.S. bridge collapse data (Compiled after Imhof 2005)

Bridges age with time and need to be repaired, rehabilitated, or replaced when they are not qualified for service in the public transportation system. To assist bridge managers to better manage their bridges, the state governments, the Federal Highway Administration (FHWA) of the U.S. Department of Transportation (USDOT), and the American Association of State Highway and Transportation Officials (AASHTO) developed the federal and state bridge maintenance and management program (Hearn et al., 2002).

However, despite their efforts, there are realistic constraints and challenges that face bridge maintenance and management program, including increased traffic flow and insufficient funding to sustain an effective bridge management program. According to the reports from state highway agencies, in 2012 the traffic volume per vehicle miles is reaching 2,946 billion miles on all roads and streets, which is equivalent to a 56.2% increase when compared to the traffic volume in 1987 (FHWA, 2012). The increased traffic has caused great pressure to the public transportation system. Consequently, increased transportation uses accelerate the aging of bridges, frequent inspections and maintenance works are required to ensure the safety of the bridges. The limited bridge funding is an issue that constrains the effectiveness of existing bridge maintenance program. The ASCE 2009 report card pointed out that almost 40% less funding are available every year for bridge repair when compared to the actual bridge rehabilitation needs (ASCE, 2009).

This dissertation addresses yet another constraint: the lack of cost-effective and qualitative inspection technologies for highway bridges has also become an apparent limiting factor for achieving a highly effective nationwide bridge management system

(Orcesi & Frangopol, 2010). An effective bridge management system requires precise and accurate bridge condition data and can help minimize unnecessary expenditures, result in cost saving to the DOTs. Therefore, research that result in quality bridge data can enhance bridge management.
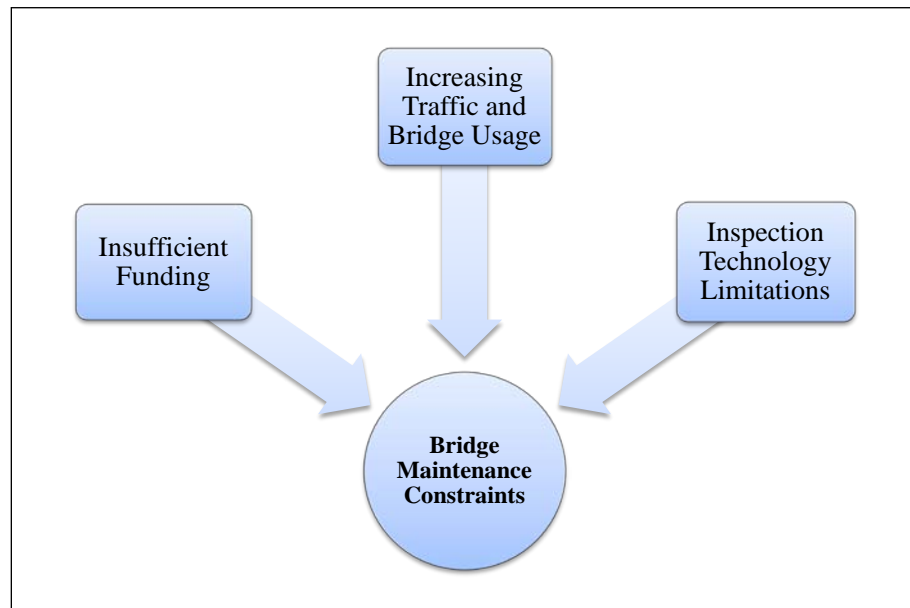
Figure 1.2 Constraints of building an effective bridge maintenance system

Figure 1.2 summarizes the discussed constraints to an effective bridge maintenance program. Current research specifically addresses the inspection technology issue by suggesting the use of remote sensing technologies for bridge inspection. The bridge inspection regulation has been addressed in the "Federal Highway Act of 1968" as a national standard for bridge administration. Current National Bridge Inspection Standards (NBIS) mandates that all public highway bridges in the U.S. are required to be inspected at least once every two years. There have been several recent studies discussed about whether this interval is sufficient (AASHTO, 2009). However, a more critical issue regarding bridge inspection may not be related to how frequent the inspection is conducted, rather be about the quality of bridge data that is being collected.

1.2 Classifications of Bridge Inspection

The techniques used to inspect bridge conditions can be generalized into two categories: global and local inspection techniques. Global inspection (Chang et al., 2003) studies the overall characteristics of a bridge structure, while local inspection (Karp et al., 2008) focuses on the problems of specific bridge components. Current visual inspection technique, for example, is a component-based method that divides the bridge into components and substructures (FHWA, 2004).

Vibration testing or dynamic characterization and static load tests are techniques that can be employed for global bridge inspection. Vibration testing combines knowledge in system identification, vibration theory, vibration testing, as well as data acquisition and analysis has been widely applied to bridge inspection to evaluate the health state of a bridge structure (Wang et al., 1997). For example, experimental modal analysis (EMA) has been suggested for global structure inspection (Ren et al., 2004).

Localized inspection (Ko & Ni, 2005) can help bridge inspectors to pin-point small-scale damages in a bridge structure, it provides better understanding of the bridge mechanical characteristics, and it can be used to predict potential problems. The most common local techniques used in bridge inspection include but not limited to ultrasonic, dye penetrant, magnetic particle, acoustic emission and infrared imaging detection, etc.

1.3 Visual Bridge Inspection

Visual inspection is currently the primary method performed for highway bridge inspection. During visual inspection, the inspection team needs to walk to the site and observe the bridge conditions to find out bridge defects following the federal or state

bridge inspection procedures, and input the inspection data into the bridge management software (BMS).

The DOT bridge inspection workflow is as follows: initial inspection scheduling, agency selection and contracting, field bridge inspection, data processing, and reporting (Mills & Wakefield, 2004). Visual inspection is performed in this workflow during the field inspection stage. NBIS visual inspection categories detailed the list of bridge components for surveying when processing bridge inspection data.

Table 1.1 NBIS inspection components

Types of Inspection	Inspection Points
Approach	Vertical alignment and slope
Deck	Wearing surface
Superstructure	Beam, surface and plate
Sub Structure	Cap, column, undermining and slope
Signage	Required sign, posting
Channel	Debris, flooding, change in the channel

1.4 Proposed Solution: LiDAR for Bridge Inspection

LiDAR (laser scanning) technology has been proposed for bridge inspection (Liu et al., 2009). The objective of current study is to address several advanced topics including: technology evaluation, bridge inspection workflow implementation, and data collection quality management. These topics are deemed critical to guarantee quality data for implementing LiDAR in actual inspection process.

The study of LiDAR scanning principle is important to determine whether it is capable of measuring problems associated with the bridge inspection elements. Laser ranging can be an ideal method for bridge survey, because it can conduct precise range measurement regardless of the changes in weather or light conditions. In this study, experiments have been conducted in the field as well as in the laboratory. Those

experiments will provide persuasive data regarding the performance of the technology for bridge inspection. It is believed that bridge service life can be extended once LiDAR technology is used to provide quantifiable inspection data to bridge managers. For technology implementation, capital investment is required to purchase laser equipment, train inspector, and develop software. Thus, the comparative cost analysis is performed to determine the potential of LiDAR technology implementation.

Introducing LiDAR technology to bridge inspection will have direct impact on current inspection procedures. Before the LiDAR use, the inspection teams have to go to the site and check the bridge condition visually. Once the LiDAR is used during inspection, they can operate the scanner and reduce the inspection time on site. The superior features of the new technology allows the team to complete a simple scan in 5 minutes, which means a significant change in the time allocated for field-testing and post scan data processing. Current inspection reporting system deals mainly with documents, literal reports, as well as small format pictures, but the use of LiDAR will add large number of data into the system. The reporting system is recommended to make changes to accept point cloud data (about 100 MB for 1/4 resolution scan) in the transmission, which indicates that the network and database need to be improved accordingly.

The reliability of bridge inspection data is important in bridge management, because the low quality inspection data will mislead the managers. In order to ensure the data quality in bridge inspection, FHWA (2005) has established an inspection framework to provide a systematic quality management solution for visual bridge inspection. One of the typical quality issues of visual inspection is the inspection team sometimes need to disturb the inspection priority of different bridge components and damages, thus they do

not have sufficient field time to examine the important parts. Another issue is that subjective judgments could lead different views of the same bridge issue from different inspectors.

1.5 Scope of Work

During the course of this study, over 100 bridge scans have been performed. Selected data are then used for this study. The first step in this study is to revise the computation algorithm and determine approaches to improve the accuracy and proficiency of the previous damage detection algorithm. Potential error sources in LiDAR bridge damage quantification are studied, specifically, the scanning angle influence is addressed. Next is to apply the reflectivity data to improve the damage detection ability. Case studies using LiDAR bridge inspection to study the bridge joints condition and simulated embankment deformation by environmental changes is presented as an extension to the bridge inspection applications. The following research objectives have been established to complete this research:

- Develop and verify the improved damage quantification algorithm.
- Study the scanning angle effects on LiDAR damage quantification.
- Study the inclusion of reflectivity data into damage detection to enhance the defect identification.
- Investigate bridge joint evaluation using LiDAR inspection technology.
- Study the performance of LiDAR inspection in monitoring simulated slope stability.
- Quantify LiDAR technology implementation potentials.

1.6 Organization of Dissertation

The dissertation is organized in the following order: The second chapter reviews literatures on point cloud processing, Delaunay's triangulation, and edge detection in image process. The third chapter is about how to improve the defect quantification algorithm. Automatic reference plane generation (using minimum mean square error) and Delaunay's triangulation for defect quantification will be presented in this study to enhance the technology's performance in bridge local damage detection. The algorithm will be tested and evaluated using selected sample data from actual bridges. Scanning angle effect will be studied to determine as a possible critical error source when conducting a scan test, in order to find out how scanning angles influence the inspection results, an experiment will be designed to validate the scanning angle effect. The fourth chapter: the reflectance value will be included into the damage identification algorithm to enhance the capability in the recognition of certain types of defects. It is desired to resolve problems in recognizing damages in curved surfaces and defects or crack returns with insufficient scan points. The fifth chapter: besides developing specific inspection algorithms, the practical approach in using LiDAR inspection to evaluate the bridge deck joint conditions will be conducted. Considering LiDAR has already been used for geological survey, the possibility of using this technology to monitor the bridge embankment will also be studied. An experiment will be designed to simulate the rainfall erosion effects on slope stability using fly ash, and the loss will be measured using LiDAR inspection algorithms. The sixth chapter is a detailed discussion about quality issues in LiDAR bridge inspection, the error sources of this technology will be analyzed and the potential of using quality management in enhancing the inspection data quality is

also studied. The seventh chapter: conduct comparative cost analysis on the implementation of LiDAR bridge inspection for Mecklenburg County, North Carolina.

1.7 Anticipated Outcomes

The proposed study is anticipated to achieve the following outcomes:

An enhanced LiDAR damage detection algorithm, which using the spatial information from the scan data also with automatic reference plan generation then an improved quantification algorithm will be presented.

Reflectivity from the LiDAR scan will be included to the damage detection program to identify defect parts in curved and other complex bridge surfaces.

Edge detection can assist bridge deck joint evaluation by using LiDAR technology. It will be established as an important extension for bridge inspection. Besides, the attempt of monitoring the bridge embankment deformation by using LiDAR will also be made.

The issues of LiDAR bridge inspection implementation are also studied in order to provide suggestions to introduce this technology to the DOT bridge maintenance divisions.

CHAPTER 2: LITERATURE REVIEW

2.1 Quality Issues in Visual Bridge Inspection

Current study is based on the fact that visual inspection alone is not sufficient for obtaining precise bridge data for effective management of bridges. This fact recognizes that potential errors can impact visual inspection results. Systematic error means the misinterpretation between physical phenomena and visual inspection results. Moreover, variance from inspector's personal perspectives (subjective judgment), and errors in data collection and processing all having impacts on the inspection results (Dietrich et al., 2005 and Moore, et al., 2001)

It is important to improve bridge inspection data quality, because it is the foundation of effective bridge management operation. Bridge inspection data is essential in determining how to perform bridge maintenance, repairs, rehabilitations and replacement of a bridge. Effective bridge management necessarily means optimal allocation of limited maintenance resources.

FHWA (2005) has adopted systematic quality management framework to ensure visual bridge inspection data quality to minimize errors during data generation. The framework recommends documenting the entire QC/QA program, and then developing the recommended bridge inspection manual accordingly. The specific directions for QC/QA operations of bridge inspection are designed to guarantee data quality by the

framework. Figure 2.1 shows the recommendations for data quality management within the FHWA framework.
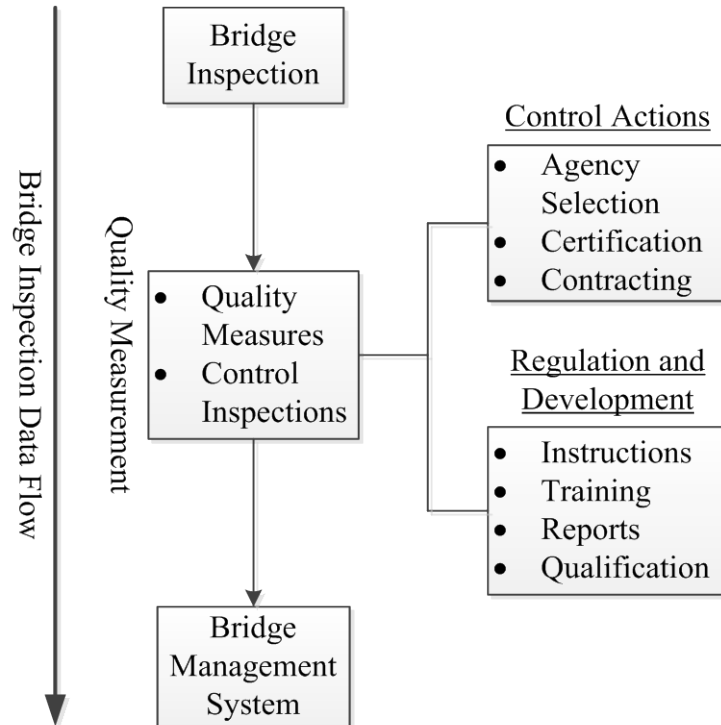
Figure 2.1 Data quality management in bridge inspection (Dietrich et al., 2005)

Regarding the improvement of current bridge inspection data quality, the researchers put forward two suggestions: optimize current bridge inspection quality management framework, or develop advanced inspection technologies to supplement visual inspection.

2.2 Sensing Implementation

Farrar et al. (2001) introduced an integrated structural health monitoring system, which was developed for monitoring weld connections in steel moment-resisting frame structures. The system consists of data acquisition equipment and software analysis.

Wireless sensor network was developed to solve maintenance problems associated with the wiring of sensors to wire-based data acquisition system.

Strain sensors have been used for long term inspection and monitoring of the structural degradation in public civil infrastructures. Strain sensors are sensitive to the change of the intensity of forces caused by structure deformation, cracking, and other related damages. Strain gauges are widely used for its convenient, low cost, firm and impervious joint.

Recently, the researchers also attempt to find alternative sensors and materials that can substitute strain gauges (Chan et al., 2006). Similar to strain gauges, optic fiber Bragg-grating (FBG) strain sensors were embedded into reinforced concrete, or weld to steel structures to monitor the variation of the strain. A fiber-reinforced polymer (FRP) composite is used to protect the optical fiber when breakage occurs. One of the problems with this technology is that it is often applied to new structures, because these sensors have to be embedded into the structure before the construction is completed. Therefore, it is a not practical method for monitoring existing structures, because installation is costly and challenging.

Yan et al. (2010) developed a highly accurate corrosion sensor: the signal energy of sensors shifts from low frequency to high frequency during a corrosion process, and this feature is used to monitor the corrosion. This technology could be used along with environmental sensing methods such as temperature, humidity and acid level, to evaluate the corrosion status of structures.

All the above mentioned bridge monitoring technologies have some common limitations when applied for bridge management: they are costly considering the limited

bridge findings and current low cost manual inspections. Moreover, an extensive technical knowledge is required, and it is challenging to collect and analyze the field inspection data when using those localized inspection technologies.

2.3 Remote Sensing for Bridge Inspection

Commercial remote sensing (CRS) and Spatial Information (SI) have been introduced to bridge inspection and management (Liu et al., 2009). Bridge information acquired from commercial remote sensors can be used for both global and local inspections (Ribarsky et al., 2009). Remote sensing technologies are a convenient way to bridge health monitoring by gathering high-resolution images and wide-bandwidth spectral information for bridge condition evaluation (Chaudhuri & Samal, 2008). For example, high-resolution image can be used for global inspection bridges, and the imaging can be performed from distance away. Moreover, with the improvement of the optical resolution of the remote sensing technology, the imagery could be used to identify small defects.

Remote sensing technologies are able to cover a wide range of area, gather large amount of information and provide repeatable data. More importantly, it provides reliable documentation of a bridge for inspectors to review and evaluate for maintenance planning. However, there exist several issues for remote sensing technologies implementation including: the lack of formal guidelines in regulating the use of remote sensors for bridge management; bridge managers are usually unfamiliar with the technology and the inspection platforms, and the processing of image data can be a challenge when applying remote sensing in bridge inspection (Chen, 2010).

Light detection and ranging (LiDAR) is a precision measurement tool, which uses laser light to measure distance (Boehler & Marbs, 2002). It emits laser beams of certain wavelength and detects the time to return of the laser beam. The distance is then calculated through multiplying the speed of laser light with the travelling time.

Laser scanner creates a 3D coordinate system with its own position as point (0, 0, 0) and record the relative position of the surrounding targets. It also records the reflectance value of each returned scan point along with the coordinates. The reflectance value is the direct measurement of the intensity of the returned laser energy, and the coordinates give the spatial information of each scanned points. Laser ranging could be conducted by three different measurement principles: time-of-flight, phase-shift, and triangulation. They vary in precision, measuring range, and recording format. The triangulation scanner is mainly used for precise distance measurement within 2 meters range, so it is not often used in civil work projects. The time-of-flight and phase-shift principles can be used in geological survey and architecture archive, because of their capability in long distance measurement capacity.

For time-of-flight measurements, a pulse of laser light is emitted towards the target and recorded at that same instant. The laser pulse lasts only a few nanoseconds and usually distributed in a Gaussian manner (Wagner et al., 2006). After traveling through the atmosphere, the laser beams reach the target, and then part of them will reflect back to the scanner. The built-in pulse receiver will detect the returned signal and the time of arrival is also recorded. Figure 2.2 shows the principle of time-of-flight laser ranging systems (Wagner et al., 2006 and Duong et al., 2006).
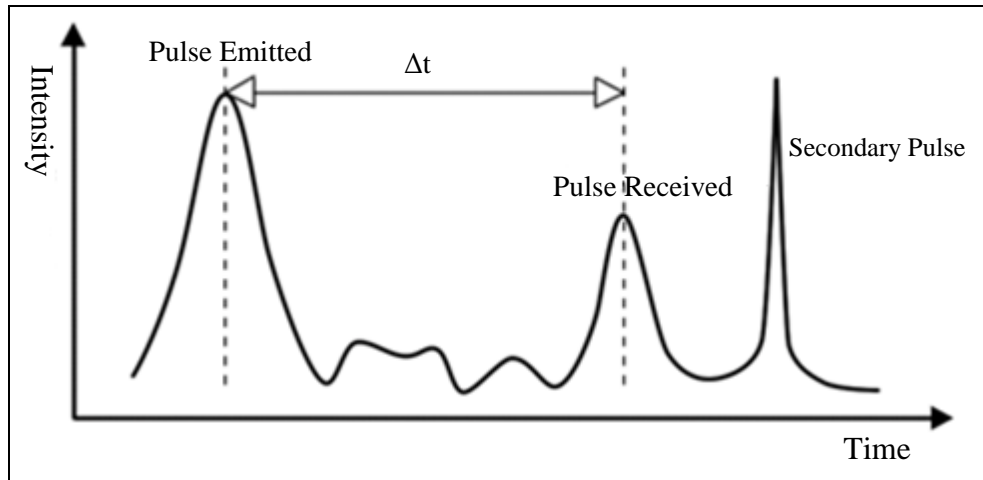
Figure 2.2 Time of flight laser ranging principle

Therefore, time t from the pulse emission till back to the scanner can be obtained, and the range R between the scanner and the object can be calculated as:

$$R = \frac{c*t}{2}$$ (2-1)

where c is the speed of light.

The performance of time-of-flight system is mostly dependent on how accurate the round trip time is measured. In other words, the pulse receiver has to be sensitive enough to capture the returned signal. In theory, the scanner is able to acquire centimeter level precision in typical measurements, but this precision is difficult to be achieved in survey projects. One effective way to maintain a high accuracy when conducting long distance measurement is to increase the emitted laser power. However, the systematic errors are still persistent, and will prevent the scanner from achieving a high precision level even with increasing its laser power (Pfeifer & Briese, 2007).

Phase shift laser scanner also sends out laser beams towards the target and determines the distance by using the reflected signals. The phase shift scanner is different from the time of flight scanners, because it will modulate the emitted laser energy into

sinusoidal signals, and then compare the phase differences between the emitted and returned signals to compute the round trip time. Therefore, the range can be calculated using equation (2-2):

$$R = \frac{1}{2} * \frac{c*\Delta\lambda}{2\pi*f} \qquad (2\text{-}2)$$

where $\Delta\lambda$ is the change in wavelength of the laser beam.
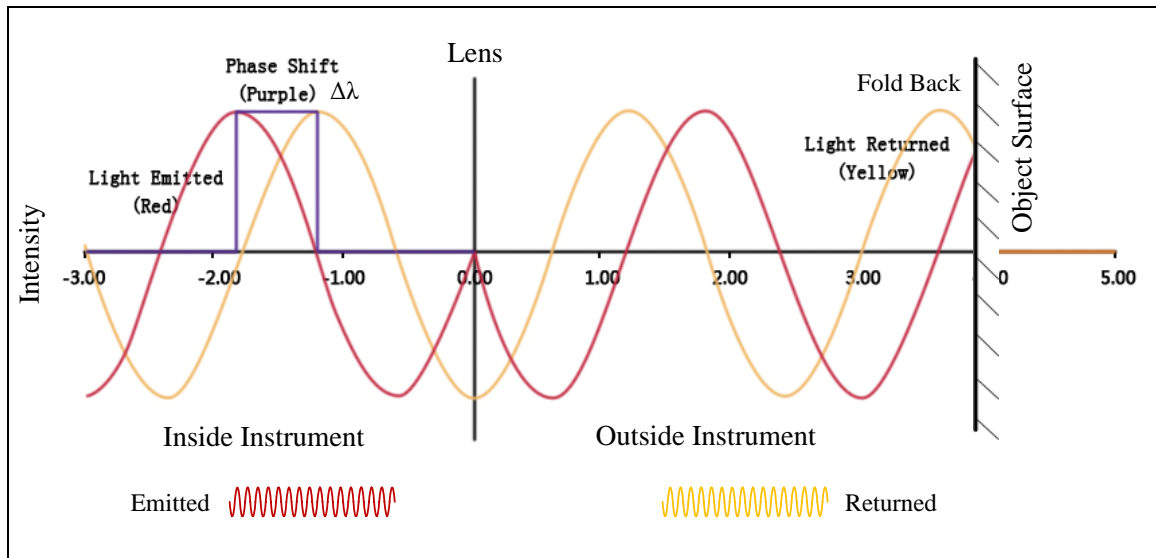
Figure 2.3 Phase shift laser ranging principle (Faro, 2007)

Phase shift measurement is more precise than time-of-flight, because the round trip time determined by phase shift comparison is more accurate than the time-of-flight method. However, there are two problems exist when using phase shift measurement: one is the measurement range is limited to half of the modulated signal wavelength ($\lambda/2$), and any distance farther than $\lambda/2$ will still get the same result in [0, $\lambda/2$]; the other problem is the measurement at unique points (n * $\lambda/2$) will return 0, because there is no phase difference between emitted and returned signals.

In order to solve this problem and make the phase shift principle applicable for engineering projects, the scanner must first modulate the laser lights into several different

wavelength signals, and then compare the phase differences of those individuals emitted and returned signals, respectively. In the end, the largest wavelength signal is used to determine the distance, while the smallest one is used to determine the accuracy. For instance, the laser signal is modulated into three different wavelengths (1.2m, 9.6m, and 76m) for Faro LS880 scanner.

Both of these different laser-ranging principles are applicable for most civil engineering survey projects. Time-of-flight laser scanner can cover a wide area due to its long measuring capability, while the phase shift scanner can conduct the measurements more precisely. Alonso et al. (2011) made a comparison of the performance of time-of-flight and phase-shift 3D laser scanners in heritage recording for the archive of the Pantheon of Kings in San Isidoro (León, Spain).

2.4 Previous Research in LiDAR Bridge Inspection

The bridge inspection of this study is mainly focused on local damage identification, which means the measurement precision is the most important factor in considering the instrument. The phase shift scanner can provide approximately 3 mm precision (at 25m) and the high dense point cloud data collection is able to assist the post scan data processing. Besides, the phase shift scanner is able to cover the highway bridges with the 76m measurement range.

Liu (2010) discussed possible advantages of light detection and ranging (LiDAR) technology for bridge inspection and suggested LiDAR scan supplementing current visual inspection. The preliminary computer algorithms using LiDAR data in bridge damage detection and clearance measurement have been developed. The concurrent experiments also show the possible benefits of this technology. It is believed that LiDAR

is an effective instrument in providing bridge engineers with sufficient data for quantitative inspection purposes.

In addition, Liu also presented a terrestrial LiDAR bridge evaluation system, which is capable for bridge surface defect detection and quantification, clearance measurement, and displacement measurement. After taking a series verification tests in Mecklenburg County, North Carolina and other areas, along with a cost-benefit analysis, From technology prospective, LiDAR scanner is able to acquire full 3D surface information of the target bridge, and generate dense point cloud as well. The applications of terrestrial LiDAR for bridge health monitoring can be developed with the collected 3D spatial and reflectivity data.

The vertical clearance measurement of highway bridges was usually conducted manually with surveying equipment and measuring rods. The disadvantage of this method is that it is time consuming and the result is subject to human errors. The Connecticut DOT developed a multi-laser device with three sensors and mounted on a vehicle to determine the bridge vertical clearance (Lauzon, 2000). Their report indicated this multi-point moving measurement is capable for the vertical clearance measurement from the result of 17 tested bridges. The most remarkable feature of LiDAR clearance measurement is that it can access the entire bridge deck and road surface to determine the vertical clearance and the result is accurate without subjective factors from bridge inspectors (Liu, 2010). Figure 2.4 is the result of LiDAR bridge clearance measurement under a highway bridge in Iowa, and the red line is the lowest vertical clearance of this bridge.
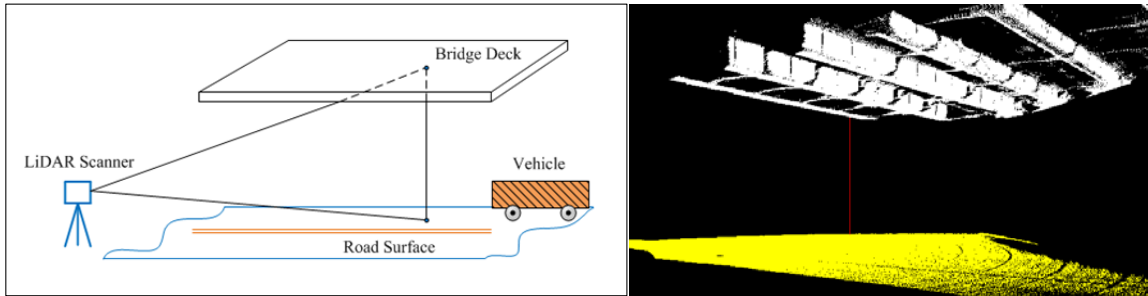
Figure 2.4 Application of LiDAR based bridge clearance measurement

Bridge damage quantification is more complicated than clearance measurement, for the damage type varies from one bridge to another. Visual inspection is capable for the detection of most bridge surface damages such as section loss or cracking, but again it is time consuming and inaccurate for the visual inspection to quantify these damages. The visual method is not able to inspect inner damages of bridge components, while some non-destructive testing technique can assess the interior of a structure. Figure 2.5 shows the bridge surface damage detection using LiDAR technology for a highway bridge in Florida.
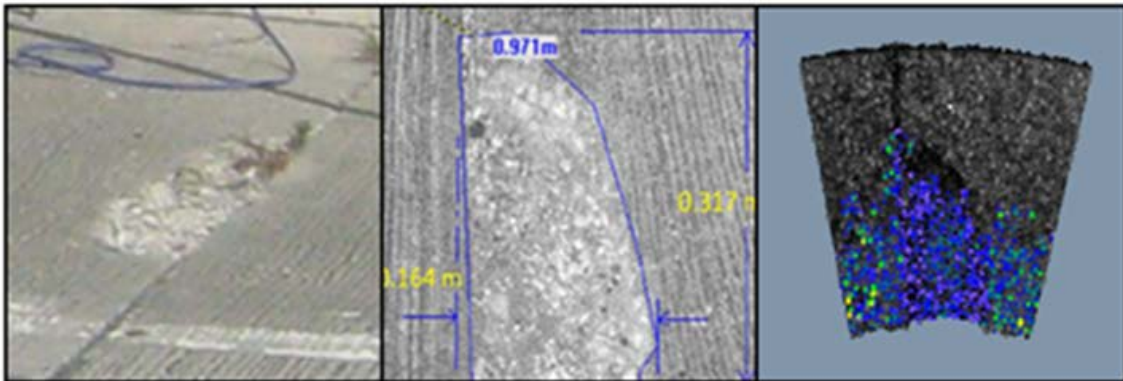
Figure 2.5 Application of LiDAR based damage detection

2.5 Data Processing for Bridge Inspection Techniques

The reason for reviewing data processing techniques for bridge inspections is that all these methods tend to employ advanced detection technologies to collect bridge inspection data on-site and then analyze the data after the inspection.

Most of the previous works aimed at establishing automated damage detection instead of relying on human observations during bridge inspection are based on photography imaging technique. For example, image processing and pattern recognition techniques are considered to be the most promising solutions to surface crack identification and defect detection. Numerous efforts have been devoted to design computer algorithms in automatic bridge surface damage identification from images. Oliveira and Correia (2012) introduced an integrated line-scan, high-speed camera and a laser system for automatic crack detection and classification using survey images acquired in a high speed vehicle. Besides, they used the damage extraction approached in the automated system which is essentially relying on camera shots. To automate the determination of deterioration level during bridge inspection, Abdel-Qader et al. (2003) compared four kinds of edge detection techniques for crack identification and recognized that fast Haar transform (FHT) is more reliable for edge detection for bridge surface cracks than the other three techniques: Sobel, Canny, and fast Fourier transform.

For bridge inspection and condition evaluation that reply on image processing, image quality is an issue when trying to get accurate result from those blurry pictures. Lertrattanapanich and Bose (2002) suggested that forming high-resolution image from low-resolution images usign Delaunay triangulation to interpolation can get high-resolution images.

Li et al. (2011) raised a creative idea that use Delaunay triangulation to express the density features of the singularity points of sub sections in pavement crack pattern recognition. These are the only few cases that Delaunay triangulation has been used in constructing the patterns for automatic image identification purposes.

For point cloud data processing, the most common technique is to perform change detection through comparing the cloud data to a reference plane, which could either be the original documented scan or later virtually constructed virtual model (Girardeau-Montauta et al., 2005). In structural health monitoring, the 3D format documentation of LiDAR can be used to determine its deterioration or deformation.

The limitation of these point cloud data processing technologies are that they only deal with coordinates information. For many of applications, this coordinates-based data processing approach along is able to provide useful solutions, which include Liu and colleagues' contribution in the initial state of LiDAR bridge inspection. But the point cloud is actually numerous sets of data that contains no object information (Ackermann, 1996).

Axelsson (1999) indicated that additional sources of information outside of the point cloud data can be used to improve the processing of laser scanner data. Their research is to detect buildings from airborne laser ranging data, so they suggested adding reflectance data or multiple echoes from LRF, images, existing 2D GIS database, and land-use maps to assist the classification.

Airborne LiDAR has been used for both bridge damage detection and quantification with reconstructed topography, which comes from the XYZ coordinates for numerous returns. Haugerud and Harding (2001) conducted the analysis of error

sources for topographic construction in airborne LiDAR applications, where the measurement, classification, and interpolation errors are the most important factors.

CHAPTER 3: LIDAR BRIDGE INSPECTION PROCESS ANALYSIS

3.1 Introduction

Terrestrial LiDAR scanning data point contains fundamental information about the scanned target including: row and column number, position data, Cartesian coordinates, and reflectance value. Figure 3.1 assuming a scanned data set has n points, the set can be described as:

$$P = \begin{bmatrix} x_1 & y_1 & z_1 \\ x_2 & y_2 & z_2 \\ \vdots & \vdots & \vdots \\ x_n & y_n & z_n \end{bmatrix}, R = \begin{bmatrix} r_1 \\ r_2 \\ \vdots \\ r_n \end{bmatrix} \qquad (3\text{-}1)$$

where P is the Cartesian coordinates of the scan points, which measures the relative position of the scanned points to the scanner. R is the reflectivity value where darker scan points are usually associated with small reflectivity values, while brighter scan points are associated with higher values. The integration of all these scan points generates the 3D image of the recorded bridge structure. The evaluation of these fundamental data forms the basis for bridge inspection technique using LiDAR technology (Liu, 2010).

Current study extents Liu's work (2010) and addresses methods to improve the quality of LiDAR scan bridge evaluation. Specific issues addressed are: 1) scanning angle effect and 2) damage detection algorithm.
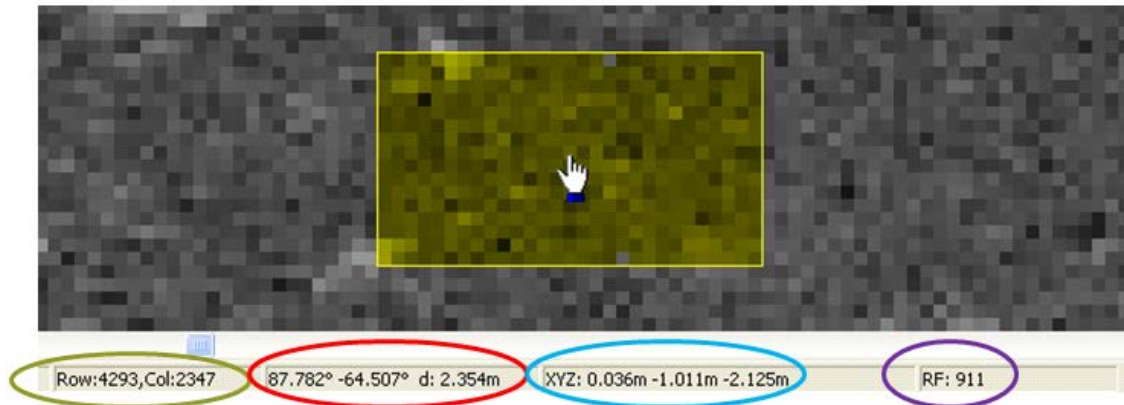
Figure 3.1 The structure of data in a LiDAR scan point

3.2 LiDAR Bridge Inspection Process

Both visual inspection and LiDAR bridge inspection belong to the 'field bridge inspection' and the 'data processing' processes, as defined in the DOT's bridge inspection workflow. Visual inspection emphasized onsite survey and measurements, where most data processing are performed off sites. Likewise LiDAR reforms onsite data recording and data processing incurs offsite. Therefore, data quality control should be addressed both in the field and offsite.

3.2.1 Field Bridge Data Collection

We envision that the inspection team will travel to the site with the laser scanner, and follow the recommended visual inspection procedures to evaluate the bridge conditions. After inspecting the bridge visually, the team will determine the necessary scan parts and determine the appropriate positions for performing the scan.

The benefit of using a laser scan is documentation of the damage, which can be quantified using the laser data. Figure 3.2 is the digital 3D reconstruction of a highway bridge in Iowa. For clearance measurement, it is suggested to place the LiDAR scanner between the bridge deck and road surface as shown in this figure. However, for damage

detection, it is better to place the LiDAR scanner close to the damage spot for higher spatial resolution scans.

Figure 3.2 3D reconstruction of LiDAR scanning data of a highway bridge

3.2.2 Scanning Angle Effect Study

Since site deployment of laser scanner may involve limited access points, the scanning angular, range, edge effects, and surface reflectivity issues may affect the scan quality. Scanning angle effect can be significantly influencing to the outcomes of damage quantification. Therefore, the following experiment is established to study the scanning angle effect in LiDAR damage detection.

To simulate the damaged bridge surface, a flat panel embedded with 6 cylindrical indentations is used in the experiment. Each of the cylindrical is manufactured with different material to simulate various surface types. The flat panel has been scanned at five different positions using LiDAR scanner, and the experiment setup is shown in Figure 3.3.
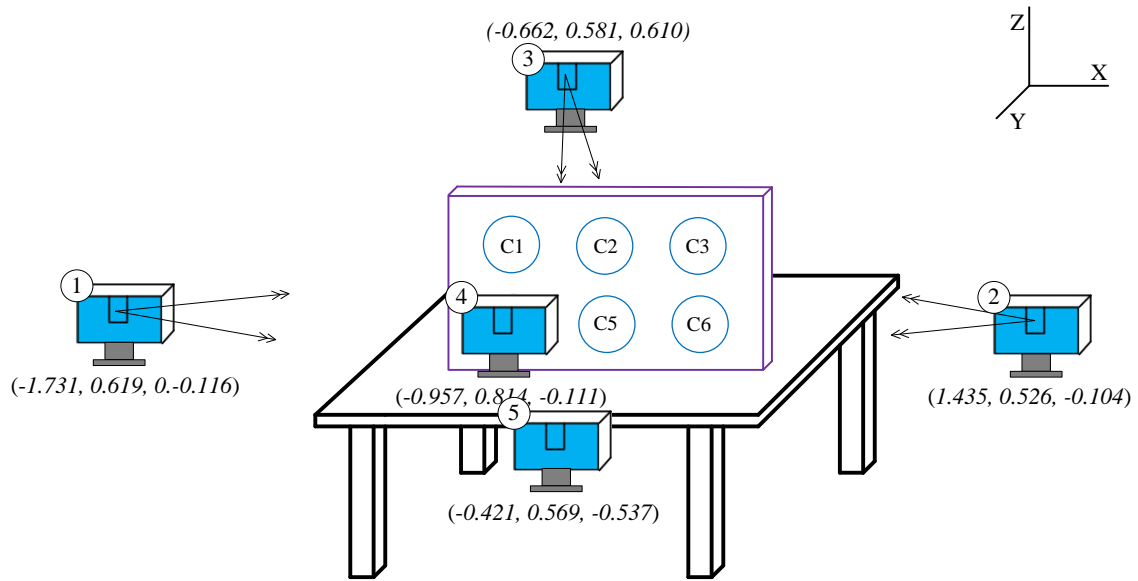
Figure 3.3 Experiment setup of the scanning angle effect study

In this experiment, the LiDAR data is analyzed using Liu's (2010) quantification algorithm. Table 3.1 and 3.2 is the quantification result of the area and volume cylindrical samples scanned from the 5 different positions.

Table 3.1 LiDAR 'defective' area quantification in the model (Unit: m^2)

Area	C1	C2	C3	C4	C5	C6
Design	8.11E-03	1.03E-02	8.11E-03	1.03E-02	1.03E-02	1.03E-02
1. Left	5.47E-03	4.20E-03	3.74E-03	8.39E-03	6.36E-03	3.42E-03
2. Right	4.41E-03	7.28E-03	8.23E-03	7.18E-03	6.40E-03	7.77E-03
3. Top	9.18E-03	9.38E-03	8.97E-03	1.69E-02	9.31E-03	9.50E-03
4. Center	9.57E-03	9.63E-03	9.09E-03	1.01E-02	1.00E-02	9.35E-03
5. Lower	9.98E-03	9.41E-03	9.67E-03	9.92E-03	9.72E-03	1.08E-02

Table 3.2 LiDAR 'defective' volume quantification in the model (Unit: m^3)

Volume	C1	C2	C3	C4	C5	C6
Design	2.43E-04	2.11E-04	2.19E-04	2.43E-04	2.11E-04	2.19E-04
1. Left	1.52E-04	9.27E-05	6.73E-05	2.25E-04	1.73E-04	7.73E-05
2. Right	1.09E-04	1.67E-04	2.05E-04	2.02E-04	1.74E-04	2.39E-04
3. Top	2.70E-04	2.18E-04	2.24E-04	3.92E-04	2.51E-04	2.77E-04
4. Center	2.92E-04	2.29E-04	2.40E-04	3.00E-04	2.85E-04	2.70E-04
5. Lower	2.96E-04	2.17E-04	2.34E-04	2.77E-04	2.59E-04	2.89E-04

The quantification result of this experiment is first related to point cloud data collection process, which determines whether the technology would record the right and sufficient information. Meanwhile, the result is also related to the computer aided data analysis process, which determines whether the defective areas would be well recognized and calculated. Table 3.3 and 3.4 demonstrate the quantification errors due to scanning angle effect.

Table 3.3 The area quantification error due to scanning angle effect

Area	C1	C2	C3	C4	C5	C6	Average	Std.
1. Left	-32.59%	-56.04%	-53.92%	-18.23%	-38.06%	-66.62%	44.75%	0.18
2. Right	-45.58%	-20.58%	1.49%	-29.99%	-37.64%	-24.28%	28.01%	0.15
3. Top	13.21%	3.55%	10.64%	64.37%	-9.26%	-7.41%	18.91%	0.22
4. Center	18.01%	8.77%	12.07%	-1.94%	-2.37%	-8.84%	8.22%	0.06
5. Lower	23.14%	2.75%	19.33%	-3.35%	-5.30%	5.03%	10.74%	0.08

Table 3.4 The volume quantification error due to scanning angle effect

Volume	C1	C2	C3	C4	C5	C6	Average	Std.
1. Left	-37.62%	-56.04%	-69.23%	-7.67%	-17.93%	-64.66%	42.19%	0.25
2. Right	-55.18%	-20.58%	-6.52%	-17.14%	-17.55%	9.04%	21.00%	0.18
3. Top	11.20%	3.55%	2.31%	61.02%	19.17%	26.73%	20.66%	0.22
4. Center	20.15%	8.77%	9.69%	23.28%	35.06%	23.53%	20.08%	0.10
5. Lower	21.70%	2.75%	7.09%	14.04%	22.83%	32.06%	16.74%	0.11

Liu (2010) has made a brief analysis of the reason that scanning angle influence happens. The primary factor is that the scans cannot be conducted exactly facing the 'damage', as a result, it is difficult to get a clear edge recording. This is because most laser lights touch the damage edge from that direction would scatter rather than return back to the scanner. Therefore, the recorded data will not get sufficient scan points for the edge area. The secondary factor is the laser light from side scans could be blocked by the

damage edge and cannot reach the entire defective surface, thus the oblique scan cannot capture the entire volume of the damage.

Figure 3.4 demonstrate the 3D reconstruction of the quantification results for position 5 (the 'lower' scan). From the experiment, we can see that the scanning angle effect could bring a considerable error to the quantification results. Meanwhile, the quantification algorithms could also lead to error in the analysis.
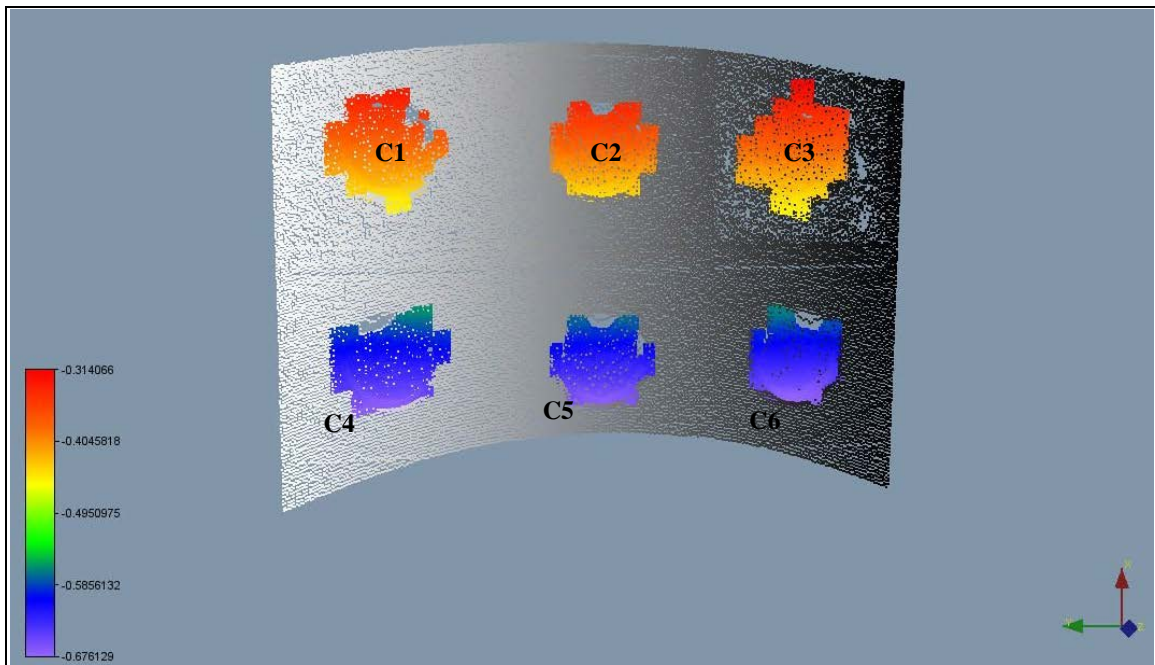

Figure 3.4 3D reconstruction of analysis result for the lower center scanning

Therefore, in order to mitigate the scanning angle effect, the LiDAR scanner has to be placed right opposite to the damage. The other possible way is to increase the outgoing laser energy from the scanner to increase the emitted laser power, and then the scanner could get enough returned points from the defective edge. But the systematic errors will still persist and would prevent the scanner to achieve an ideal precision (Pfeifer & Briese, 2007). In addition, the over emitted power could cause health issues to the operator.

3.2.3 Post Scan Data Analysis (Damage Detection)

In the post scan data analysis, the bridge condition evaluation team will use computer programs to detect and quantity defective areas, measure bridge clearance and structure deformation, which is completed through determining the changes on the 3D point cloud data of the bridge.

The most common method used to perform change detection of point cloud data is to compare it to a reference model, which could either be the original achieved or virtually constructed 3D CAD data. In bridge damage detection, the original scan is obviously the most reliable reference, and the point cloud data of defective areas can be compared to this original data. However, since most of bridges do not original laser scan data, the virtual 3D bridge model reconstruction seems to be the only approach to perform change detection.

(1) 3D Shape Reconstruction for Defective Zone

The reconstruction of the 3D shape for the defective areas in highway bridges is a challenging problem. The most essential part of the automatic shape reconstruction is to define a reference plane for the selected point cloud, which is used to determine whether there are defective areas in the point cloud.

Liu (2010) introduced a way to reconstruct the shape of the defective zone by generating a flat plane according to the boundary information of selected study area, which is an estimation of the original bridge shape. Three points from the surface of the undamaged areas are selected to determine this reference plane for the later damage quantification. In order to avoid introducing noise data the noise point when selecting

those determinate points, it is necessary to compare their coordinate values with the neighbouring points.
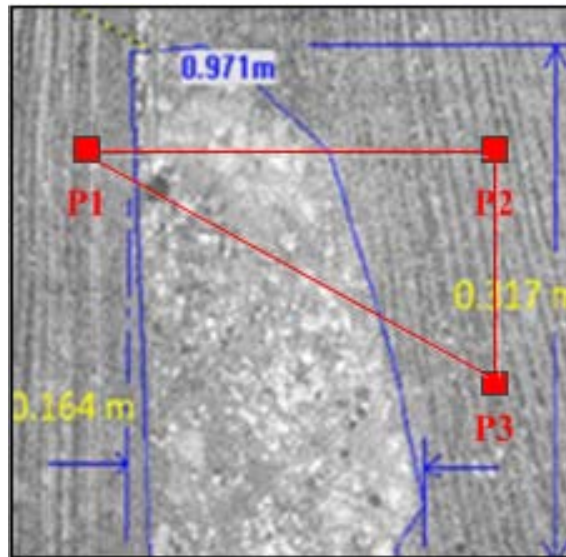
Figure 3.5 Reference plane generations in Liu's algorithm

Liu's algorithm is simple and effective, especially when the defective bridge component was laying on a flat surface. But when the damage is located on a curved surface, Liu's method is unable to reshape the point cloud data and make it close to the original condition. This algorithm is also semi-automatic and requires human interactions to select the study areas.

In order to make laser inspection automatic and more adaptive, the mean-square-error (MSE) is used to determine the reference plane. In three dimensional space, it is supposed that only one plane exists with the minimum MSE for the given point cloud. The improved algorithm requires the selection of as much undamaged area as possible to make the reference plane as close to the original surface. The MSE of the point cloud is defined as following:

$$MSE = \frac{\sum_{i=1}^{n}(d_i)^2}{n}, i = 1, \cdots, n \qquad (3\text{-}2)$$

where n is the number of the selected cloud points, d_i is the distance of point i to the reference plane. In order to calculate the reference plane with minimum MSE, a regression model has been defined:

$$z_i = b_0 + b_1 x_i + b_2 y_i + \varepsilon_i, i = 1, \cdots, n \tag{3-3}$$

where $[x_i \; y_i \; z_i]$ is the coordinate of point i, ε_i is the signed distance to the reference plane, z_i is the dependent variable, and x_i and y_i are the independent variables. Here ε_i has the following relationship with d_i:

$$d_i = |\varepsilon_i| \tag{3-4}$$

The vector $b = [b_0 \; b_1 \; b_2]'$ in equation (3.3) can be calculated from regression of the two independent variables, thus the reference plane is defined as:

$$b_1 X + b_2 Y + Z + b_0 = 0 \tag{3-5}$$

Figure 3.4 is the result of revised reference plane generation for the study of a sample point cloud data.
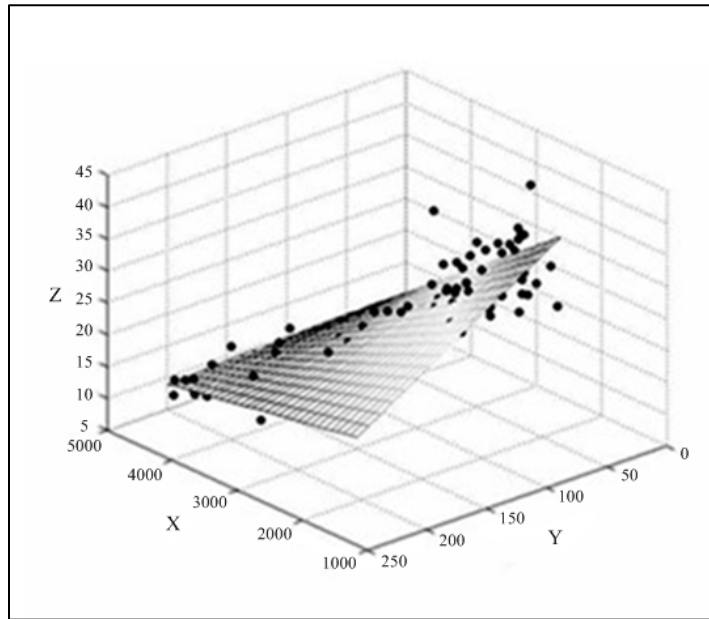

Figure 3.6 Revised reference plane generation through Min-MSE regression

In order to simplify the future calculation for damage quantification, the selected point cloud data will be mapped to a newly constructed coordinate system, where in the reference plane is parallel to $X-Y$ plane. In order to make this coordinate transformation, the following steps are suggested:

- Normalize the vector of the reference plane calculated from the regression model:

$$\begin{bmatrix} m \\ n \\ k \\ j \end{bmatrix} = \begin{bmatrix} b_1/\|[b_1 \; b_2 \; 1]'\|^{\frac{1}{2}} \\ b_2/\|[b_1 \; b_2 \; 1]'\|^{\frac{1}{2}} \\ 1/\|[b_1 \; b_2 \; 1]'\|^{\frac{1}{2}} \\ b_0/\|[b_1 \; b_2 \; 1]'\|^{\frac{1}{2}} \end{bmatrix} \tag{3-6}$$

where $[m \; n \; k]'$ is the normalized norm vector, j is the minimum distance from $(0,0,0)$ to the reference plane.

- Use matrix T to perform the transformations:

$$T = T_1 T_2 T_3 \tag{3-7}$$

$$T_1 = \begin{bmatrix} 1 & 0 & 0 & 0 \\ 0 & 1 & 0 & 0 \\ 0 & 0 & 1 & 0 \\ jm & jn & jk & 1 \end{bmatrix},$$

$$T_2 = \begin{bmatrix} 1 & 0 & 0 & 0 \\ 0 & \frac{k}{\sqrt{(n^2+k^2)}} & \frac{n}{\sqrt{(n^2+k^2)}} & 0 \\ 0 & \frac{-n}{\sqrt{(n^2+k^2)}} & \frac{k}{\sqrt{(n^2+k^2)}} & 0 \\ 0 & 0 & 0 & 1 \end{bmatrix},$$

$$T_3 = \begin{bmatrix} \sqrt{(n^2+k^2)} & 0 & m & 0 \\ 0 & 1 & 0 & 0 \\ -m & 0 & \sqrt{(n^2+k^2)} & 0 \\ 0 & 0 & 0 & 1 \end{bmatrix}.$$

where T_1 transforms the reference plane to $(0,0,0)$ point, T_2 is the rotation matrix, and T_3 is the scaling matrix.

- Expand the coordinate of point i from $[x_i\, y_i\, z_i]$ to $[x_i\, y_i\, z_i\, 1]$, and get the transformed coordinate value $[x_{ti}\, y_{ti}\, z_{ti}\, 1]$ of point i using the following transformation:

$$[x_{ti}\, y_{ti}\, z_{ti}\, 1] = [x_i\ y_i\ z_i\ 1]^T \qquad (3\text{-}8)$$

Now, the cloud point data is represented as $[x_{ti}\, y_{ti}\, z_{ti}]$ in the new coordinate system.

(2) Identification of Defective Zone

The scan points of the defective zones usually have obvious irregular coordinate comparing with the undamaged surfaces. The two search criteria: the coordinate value difference between the selected scan points and the reference plane, as well as the variation of gradient value of the scan points will be used to determine if the scan points belong to the defective zones.

Since the selected study area has been rotated parallel to the $X-Y$ plane, the distance between the scan points to the reference plane can be easily obtained as:

$$D = \left| Z_p - Z_{ref} \right| \qquad (3\text{-}9)$$

where Z_p is the Z coordinate values of the selected scan point, Z_{ref} is the Z coordinate value of the reference plane.

The variation of the gradient between scan points is also a reliable criterion in determining the irregularity of the cloud points. The gradient of a certain irregular scan point, which has a column number C and row number R, is defined as:

$$G =$$

$$\left| \frac{Z(C+\Delta,R)-Z(C-\Delta,R)}{\sqrt{\left(X(C+\Delta,R)-X(C-\Delta,R)\right)^2 + +(Y(C+\Delta,R)-Y(C-\Delta,R))^2}} \right| +$$

$$\left| \frac{Z(C,R+\Delta)-Z(C,R-\Delta)}{\sqrt{\left(X(C,R+\Delta)-X(C,R-\Delta)\right)^2 + +(Y(C,R+\Delta)-Y(C,R-\Delta))^2}} \right|, \tag{3-10}$$

where $X(C,R)$, $Y(C,R)$, and $Z(C,R)$ are the X, Y, Z coordinate values of selected point with column number C and row number R, Δ is the number of points in each pre-determined interval (Liu, 2010). This interval value can be manually adjusted to reduce the potential deviation caused by noise data. Here both the D and G values of the studied cloud points were used to determine if they were irregular. Liu used a heuristic experience-based method to set the threshold coefficients for distance and gradient criteria, the coefficients falls within a range [0.3 0.8], and was multiple with D' and G' to get the threshold value for irregularity determination.

Selected study surface will be divided into small grids before processing the irregularity check for each point. For each grid, there are two irregular rates, which are based on distance and gradient criteria respectively:

$$\theta_D = \frac{n_{Di}}{n_{all}}, \theta_D = \frac{n_{Gi}}{n_{all}} \tag{3-11}$$

where θ_D is the irregular rate based on distance criterion, θ_D is the irregular rate based on gradient criterion. N_{Di}, N_{Gi} are numbers of the irregular points within the divided grid, and N_{all} is the total number of the points within the grid. The grid will be considered as defective when both its distance and gradient irregular rates have exceeded the predefined threshold value, which is set as 0.5 for this algorithm.

It is worthwhile to note that for complex damage detection in bridge inspection, more features are necessary to be included in the damage detection. If there were five features found to express the pattern of the damage, it would be difficult to set the threshold with heuristic method. The reason is that the features may not be of equal importance, and they have different weights in determining the attribute of the studied object.

In damage quantification of flat bridge surfaces, the distance criterion is enough to identify the defective zones. Therefore, a pre-determined tolerance value is assigned in the improved algorithm before identify the defective areas. Each point i with $|z_{ti}| > |Z_{tolerance}|$ is considered as the defect point. The approach that attempts to include multi-features in bridge damage detection will be discussed in Chapter 4.

(3) Quantification of Defective Zone

Once a grid is determined as defective, its eight surrounding grids will be checked to see if they are defective. If one of the eight grids is regarded as defective, the same procedure will be applied to others until all of them have been confirmed.

The defect area can be quantified after all grids were checked according to the defined defect identification criteria. The area and volume of the defective portion can be calculated by adding up the area and volume of each defect grid.

$$V = \sum_{i=1}^{n}(A_i \cdot \bar{D_\iota} \cdot \theta_i), i = 1, \cdots, n. \tag{3-12}$$

where A_i is the defect area of the grid i, $\bar{D_\iota}$ is the average distance of the i points in the grid to reference plane, and θ_i is the irregularity rate of grid i.
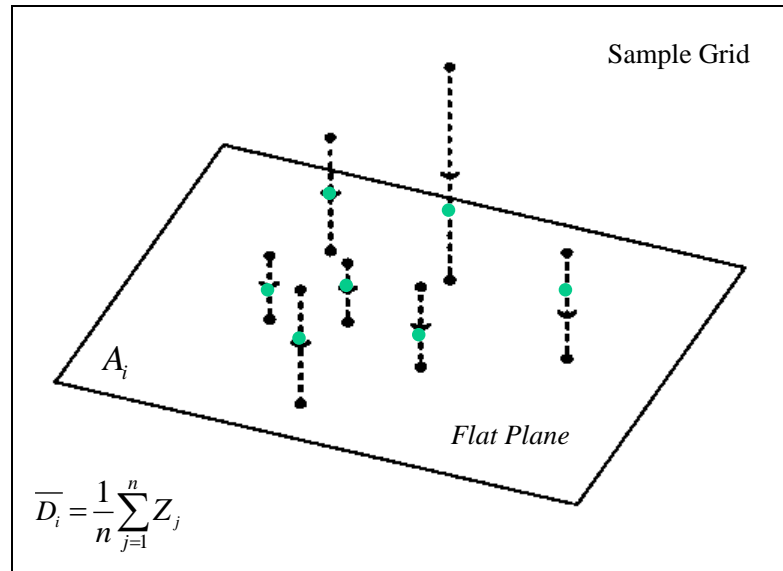
Figure 3.7 Defect identification in previous quantification algorithm

The defective mess points have no area or volume attributes, thus the formation of regular geometry using those points is necessary if quantification of the defective area has to be done. The Delaunay triangulation (Delaunay, 1930) has a clear definition according to (Shewchuk, 1999):

"Let T be the triangulation of a set V of vertices. T is called the Delaunay triangulation if and only if all triangles in T are Delaunay."

The Delaunay triangulation is used to link the scattered scan points. The following content explains the procedures for the formation of spatial surface using Delaunay triangulation.

- Project each cloud point $[x_{ti}, y_{ti}, z_{ti}]$ from the selected area onto X–Y plane.

- Use Delaunay's triangulation algorithm to aggregate the projected points into non-overlapping triangles on X–Y plane.

- Assign z_{ti} back to the projected point set, which forms a 3D surface with the triangles created in the last procedure.

The triangulation of the cloud points and the formation of surfaces in three-dimensional spaces are animated in Figure 3.8.

| ① Project 3D points to 2D flat plane | ② Delaunay's Triangulation | ③ Obtaining a polyhedral shape from the points |
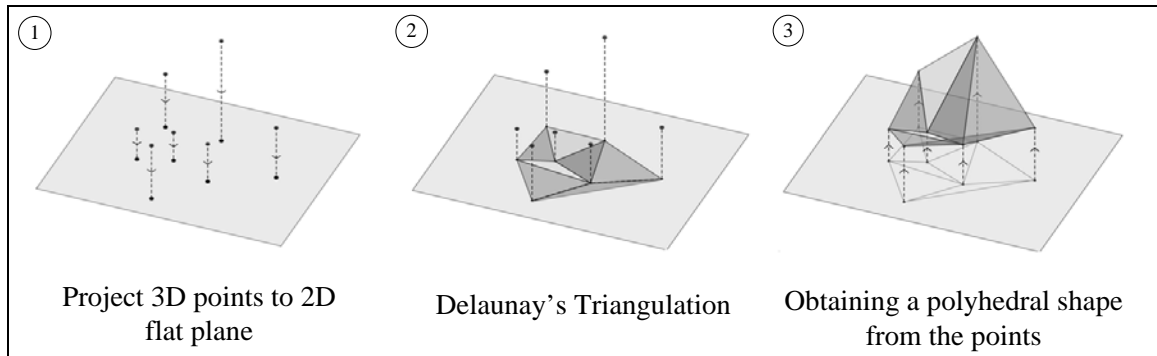
Figure 3.8 Defect quantification using Delaunay's triangulation

The area of defective zone is calculated by summing up that of projected triangles on the $X-Y$ plane, and the defective volume is then calculated by adding up the volume of those isolated triangle-prisms. The triangulation of the spatial vertices that assists the quantification of the defective zones, for the reshape of the defective portion is more close to reality if link those cloud points into triangles. It is also important to know that the interpolation algorithm used in Lertrattanapanich's research will help us for process the point cloud data where insufficient scan points returns occur.

3.3 Case Study and Recommendations

The LiDAR bridge inspection technology presented is an automatic and reliable inspection solution for surface damage quantification. It is believed as an effective tool to supplement the time-consuming visual inspection.

Bridge 590147 has been selected to evaluate the effectiveness of this inspection technology. The substructure of the bridge is showing distress in the pile caps in three areas under bridge girder. The LiDAR scan was conducted underneath the bridge, the complex damage incurred in both the bridge deck and the substructure. (See Figure 3.9).

Figure 3.9 LiDAR scan for damage detection in bridge 590147 (Charlotte, NC)

In this case study, only the defect lays on substructure will be investigated to test the revised quantification algorithm. The damage detection and quantification algorithms can outline the defective points in the spatial domain. Table 3.2 shows the result of the damage quantification using both Liu's and Delaunay Triangulation based algorithms. The percentage difference is calculated between the two different algorithms. The defective areas are shown in Figure 3.10, which are laid over the original scan and marked with different colours.

Table 3.5 The result of damage detection for bridge 590147

Area NO.	Liu's algorithm results / Delaunay based algorithm results			
	Area (m^2)	Difference	Volume (m^3)	Difference
1	1.38E-01/1.44E-01	4.3%	1.62E-02/1.73E-02	7.5%
2	1.77E-01/1.78E-01	0.6%	1.26E-02/0.62E-02	50.8%
3	1.34E-01/1.38E-01	3.0%	1.24E-02/0.33E-02	73.4%

The case study indicated that the two algorithms are very close in the quantitative results for area in bridge surface damage detection, which are highly relying on the selection of reference plane as well as the damage criteria. The obvious variances of the results in volume quantification are believed to come from the difference of reference

plane generation and the change of volume quantification algorithm (Delaunay's Triangulation).

(a). Analysis with Liu's Algorithm	(b). Delaunay's Triangulation based Analysis
Area 1	
Area 2	
Area 3	
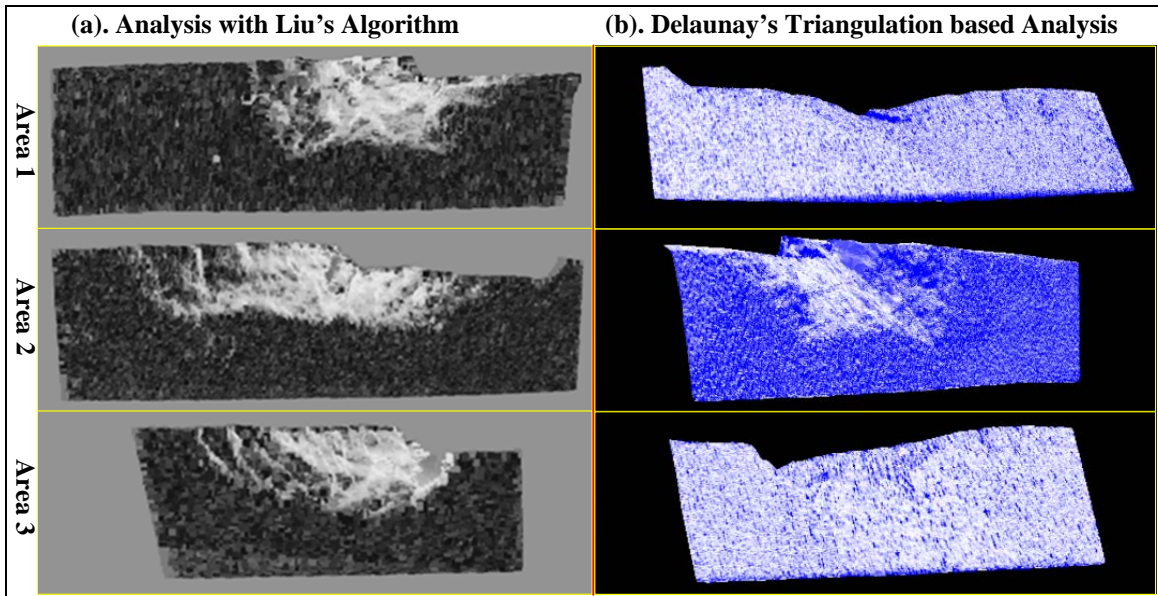
Figure 3.10 3D reconstruction of damage detection result in bridge 590147

3.4 Conclusion

In this chapter, the analysis of terrestrial LiDAR bridge inspection process has been presented. The purpose of the analysis is to study the issues that might affect bridge inspection data quality in both field bridge inspection and computer assisted data processing (automation) for LiDAR bridge inspection. With the case study presented, LiDAR technology is validated as an effective solution to visual inspection. The two issues scanning angle effect and damage evaluation algorithm are addressed and suggestions to mitigate the scanning angle effect and the improvement of the algorithms are made as well.

CHAPTER 4: REFLECTIVITY IN LIDAR DAMAGE DETECTION

Previous attempts in LiDAR damage detection essentially use the point cloud geometric (spatial) information to evaluate defects, which works with simple geometric surfaces such as flat planes or intersections of multiple-planes (Liu, 2010). To automate the damage detection procedure, additional algorithms are needed to search the defective areas. Since typical LiDAR data contains the physical geometric and the laser beam reflectivity information, this study explores the possibility of using LiDAR reflectivity to find damage areas and enhance damage detection automation.

4.1 LiDAR Reflectivity Study

According to the Phong reflection model (He et al., 1991), the surface reflects light as a combination of ambient, diffuse, and specular reflections. The light intensity actually equals to the total intensity of all three types of reflection. In a typical LiDAR scan, the ambient reflection is usually assumed to be outside of the range for consideration, thus the reflection model can be represented as:

$$I_r = I_d + I_s \qquad\qquad (4\text{-}1)$$

where I_r is the observed reflection intensity, I_d is the diffuse reflection intensity, and I_s is the specular reflection intensity.

The reflectance value of a laser beam is essentially the light intensity recording of the returning laser energy and is a function of the target surface quality, the reference beam modulation technique and the electronic phase delay. Since different surfaces may

generate different reflectivity data, the reflectivity values may help accentuate damage location.

LiDAR reflectivity has been used for post-earthquake building damage assessment (Li et al., 2009). Mass and Vosselman (1999) presented the algorithm that use sequential Hough transforms to detect building in point clouds. Similar applications that use LiDAR data, especially the reflectance value, in the research of land use or vegetarian classification can be found in several literatures. It is worthwhile to notice that, the classification algorithms in these studies are strictly limited by the instrument's resolution, and they are mostly applied to large-scale object classification. For instance, in Maas's bridge detection project, the point density of the city is 0.67 points per square meter (point spacing: 1.0-1.5m), which is a high-resolution application case as compared to the tens of meter resolution in land use classification studies.

To ensure surface damage detection can achieve a centimeter resolution, the instrument should reach a higher resolution level. The LiDAR scan has a 3mm resolution, hence, satisfies this requirement. According to Pfeifer and Briese's (2007) study in laser scanning principles, the reflectance value is related to laser spreading loss, object surface roughness and reflectivity, as well as atmospheric attenuation. The spreading loss is critical to the reflectivity value only when the laser scanning is performed from a long distance, such as airborne laser system (Baltsavias, 1999). For terrestrial laser scanner, the spreading loss and atmospheric attenuation can be ignored in the short distance transmission (Soudarissanane et al., 2007). Therefore, the surface roughness and object reflectivity are the determinants that have major impact on the reflectance values of

returned scanning points, that's the theoretical foundation of using LiDAR reflectance in detection of bridge surface damages.

The processing of LiDAR reflectance value is similar to photographic image processing, and the statistic characteristics of reflectance data acquired from the inspected bridge surface will be used to assist the bridge condition evaluation. If the reflectance values of each scan point are sorted in to a matrix R, which is actually a two-dimensional array of laser pixel intensities. The intensity value is between [0, 2047] as indicated in the manual of the laser scanner. The bridge deck showed in Figure 4.1 is selected to explain the different patterns of reflectance data distribution of different bridge surface components. In this figure, the bridge deck pavement includes normal asphalt road surface (1), roadway painting (2), and a defective area with crack distress (3&4).

In the reflectivity value histogram analysis of those three different surface types, it is clear that the reflectance values returned from normal asphalt road surface almost distributed in normal pattern, and the values are centralized to the middle of the histogram. The reflectance values returned from asphalt surface with painting nearly distributed in two isolated zones, and the values inclined to the right side of the histogram is from painting, while that near the left side is from asphalt. The reflectance values returned from asphalt with cracks have a broader distribution on the right side (high spectral), but the distribution on the left side remains the same as the normal asphalt pavement. The values are generally described as more scattered than centralized to the middle of the histogram. This example indicates that cracking and other damages destroyed the bridge surface will cause dispersion of intensity values of the returned laser lights.
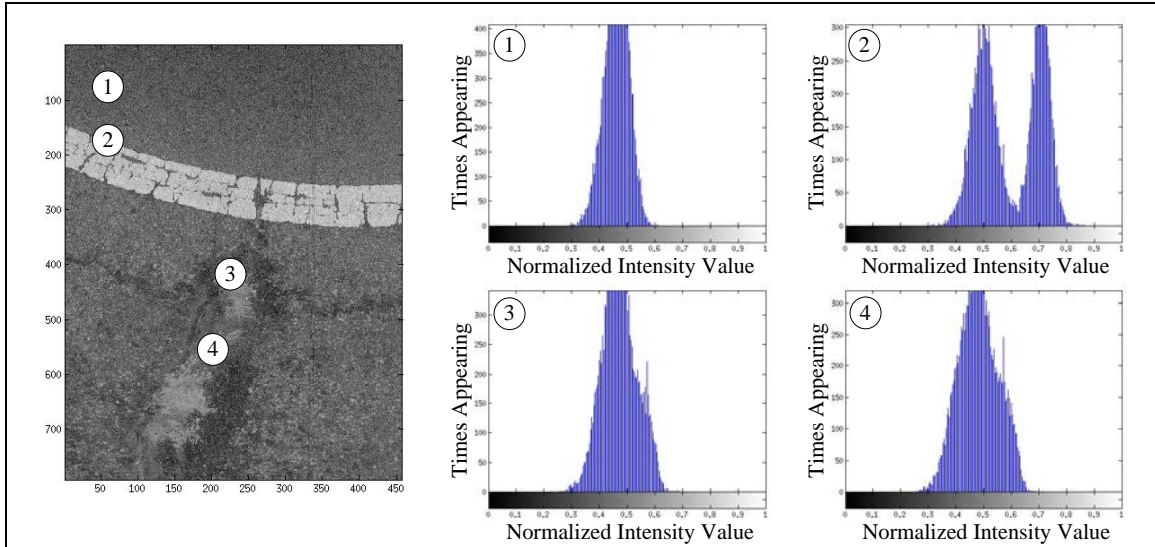
Figure 4.1 Histograms of returned laser intensity from the bridge pavement

Two-dimensional FFT is the series expansion of an image function in terms of 'cosine' image basis functions. 2D FFT is regarded as the most effective techniques in studying the frequency domain characteristics of an image, and it can filter high or low frequency spatial components from the image data for different purposes. For an image composed of M multiple N pixels, the FFT is given as:

$$F[u,v] = \frac{1}{MN} \sum_{m=0}^{M-1} \sum_{n=0}^{N-1} I[m,n] \cdot e^{-i2\pi(\frac{um}{M}+\frac{vn}{N})} \qquad (4\text{-}2)$$

where u, v is the coordinates in the frequency domain and (M, N) means the number of horizontal and vertical pixels of original image. Figure 4.2 demonstrates the Fourier Transform of an image. I[m, n] is the intensity of the point in column 'm' and row 'n'. The center of the frequency domain is the origin of the frequency coordinate system, and represents lowest frequency. The u-axis runs left to right through the center and represents the horizontal frequency, and the v-axis runs bottom to up through the center to represent the vertical frequency. The edge represents highest frequency.
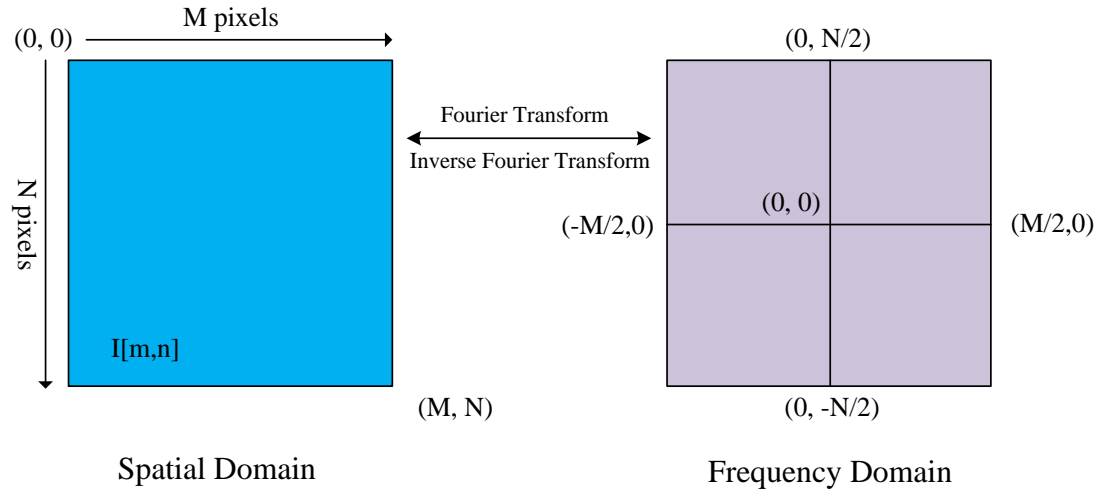
Figure 4.2 2D FFT of an image data with M*N pixels

The frequency domain characteristics of the reflectance value returned from the same bridge as studied in the histogram comparisons are investigated, which is shown in Figure 4.3:

(1) The FFT of normal asphalt indicates a neutral distribution of low and high frequency components, which means there is no sudden change of the reflectance value in the original 2D spatial domain.

(2) The FFT of asphalt with painting have more high frequency components, that came from the suddenly change around the edge of asphalt and painting.

(3) The FFT of asphalt with cracking contains even more frequency components, for the dispersion of intensity values contribute to various disorders and suddenly changes in the spatial domain.

(4) Hence, the amount of high frequency components in the FFT of the 2D spatial laser intensity would be a potential feature in the recognition of bridge surfaces.
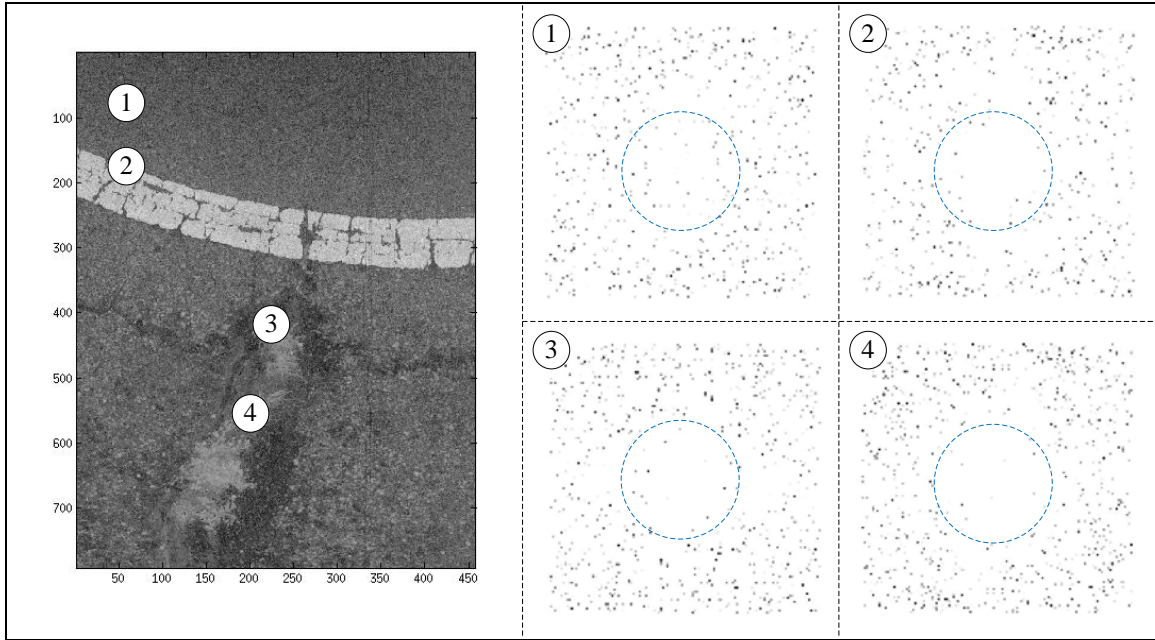
Figure 4.3 2D FFT of the returned laser intensity from the bridge pavement

4.2 Defect Detection Using LiDAR Reflectivity

The above study in histogram and FFT magnitude image patterns of the returned reflectance value from bridge surface with cracking indicates that the defective zones in the bridge surface can be detected using these two features.

The standard deviation C_{std} of the intensity values in sub matrix R_i (divided from R) is used as the expression to represent the distribution of these values. If the intensity matrix is returned from a bridge surface without defect, C_{std} will be relatively small than that of defective areas. Notice that C_{std} is relatively greater if the intensity matrix is return from surface with painting for signs as indicated in the above study.

$$C_{std} = \sqrt{E\left[\left(r_i - E(r_i)\right)\right]^2} \tag{4-3}$$

In frequency domain, the intensity image returned from normal bridge surfaces and that with defect differs in the amount of high frequency components. The mean value C_{fft} of the edge area (the high frequency components) in the FFT magnitude image

matrix M_i (transformed from matrix R_i) is used as the expression of its pattern. If the signal with a frequency greater than $\frac{f_{max}}{2}$, it is considered as 'high frequency component'. In the magnitude image matrix M_i, the 'high frequency components'' are located in the areas excluding the circle $(0,0,\frac{N}{4})$ as shown in Figure 4.4.

(0, N/2) i

(-N/2,0) $r = \frac{N}{4}$ (N/2,0)

j

(0, -N/2)
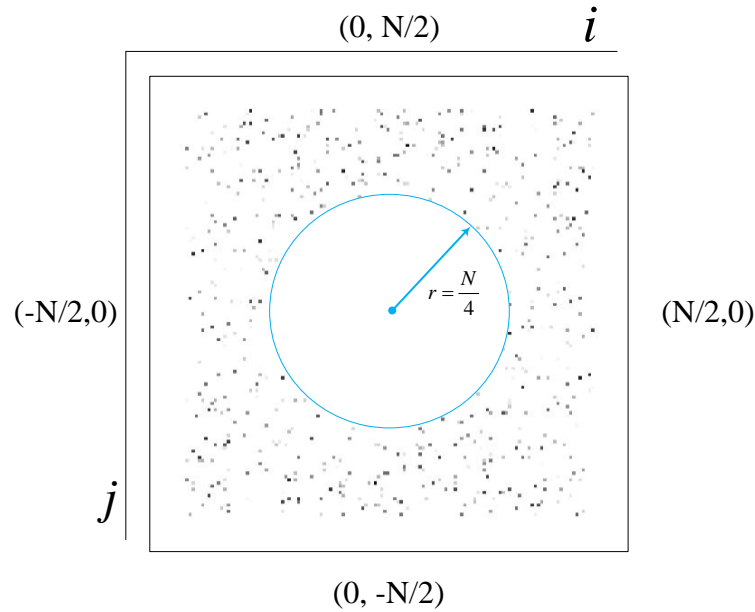
Figure 4.4 Characteristic values of the 2D FFT magnitude image matrix

The FFT magnitude image feature of the sub intensity matrix is expressed using the following equation:

$$\overline{C_{fft}} = \frac{1}{k}\{\sum_{i=-\frac{N}{2},j=\frac{N}{2}}^{i=\frac{N}{2},j=-\frac{N}{2}} I_{ij} - S_i(0,0,\frac{N}{4}) \tag{4-4}$$

If C_{std} and $\overline{C_{fft}}$ of the intensity image are used as criteria to perform damage detection in the 'bridge surface with cracking' case and set a threshold value using the experienced based method, the defective regions 3 and 4 in Figure 4.3 can be easily recognized. But when use this method for damage detection purpose in the following beam case, the result will be difficult because the intersections (1, 2, 3 in Figure 4.5) that

contains both ground surface and the beam are going to be recognized as defective during automated detection.

Figure 4.5 shows a damaged concrete placed on concrete floor As a result the two surfaces have almost identical reflection to the laser. The expression of pattern of the intersections (1, 2, and 3) is very similar to that of damage areas when using C_{std} and $\overline{C_{fft}}$, because both of them have two different major components and with significant variation of the intensity values within these sub matrixes.
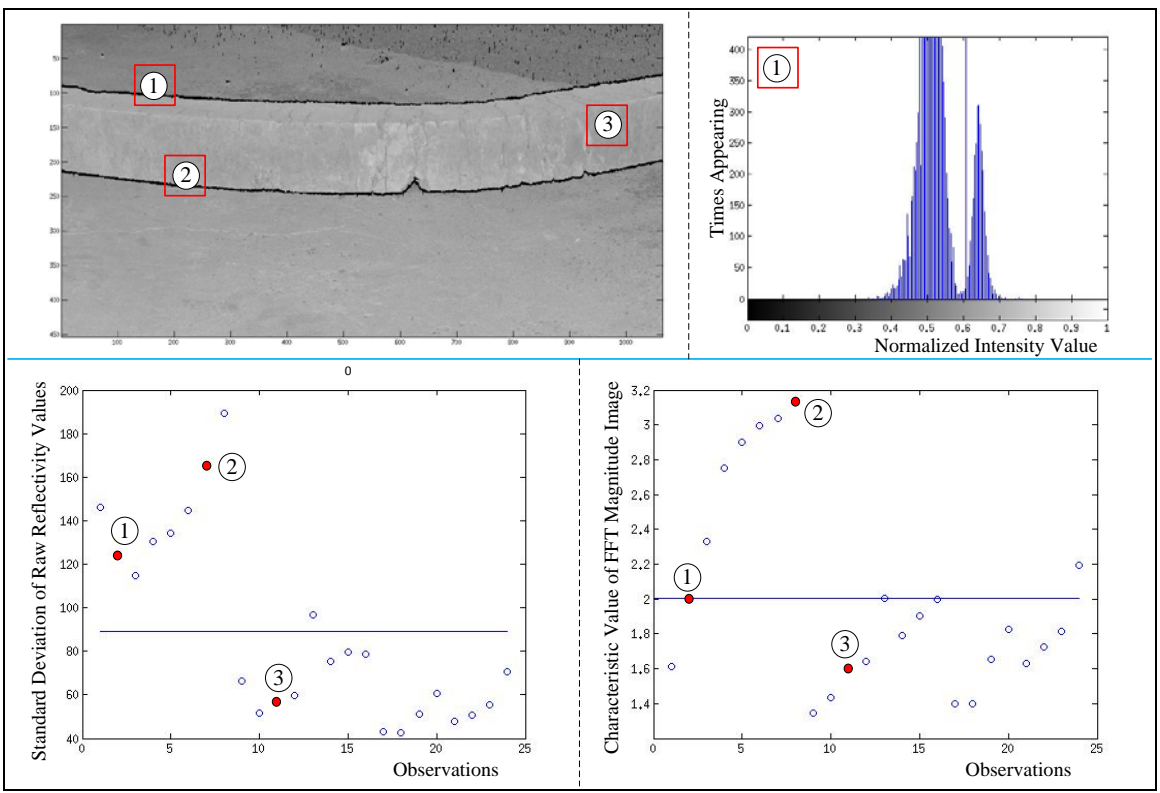
Figure 4.5 Issues when only apply reflectivity in LiDAR damage detection

Notice that in most of the studies using image-processing techniques in bridge inspection, including those listed in the literature review, they usually select bridges surface pavement to be flat and homogeneous surface to apply their various algorithms.

For damage detection in complex bridge structures, image-processing alone is not going to be helpful.

As an attempt to solve this problem, the spatial curvature of the inspection area is introduced as a feature in bridge surface damage detection. It is also possible to use curvature to indicate if the studied surface contains defective areas. For each scan point, the curvature index is defined as C_{Cur}^{ij} which compares the standard deviation of the distances from the points to its surroundings (Figure 4.6). The accumulative C_{cur} value of the points in defective zones is greater than that in the undamaged surfaces, and this could be used as one feature in the defective identification.

$$C_{Cur}^{ij} = C_1^{ij} + C_2^{ij} \tag{4-5}$$

where I, j is the column and row number of the points, $C_1^{ij} = Std\ (d_1, d_2, d_3, d_4)$, and $C_2^{ij} = \frac{1}{\sqrt{2}} \cdot Std\ (d_5, d_6, d_7, d_8)$.

The curvature expression C_{cur}^{mean} of each sub matrix is defined as the mean value of the individual C_{cur} as:

$$C_{Cur}^{mean} = \frac{1}{m*n} * \sum_{i=0, j=0}^{i=m, j=n} C_{Cur}^{ij} \tag{4-6}$$

where the divided sub matrix has m columns and n rows.
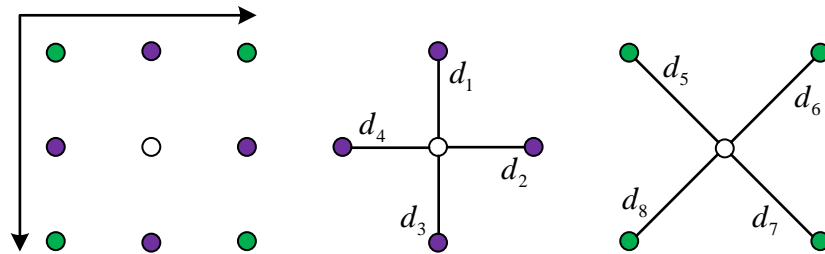
Figure 4.6 Expression of curvature feature of a single cloud point

The important thing about spatial curvature is the C_{cur} of the intersection where contains two different structure components will be extraordinary larger than that of normal surfaces and even that with defects. If the Curvature feature is used to recognize the intersections and filter them, then determine the defective areas in the rest of the sub regions, which is feasible to solve the intersection problem.

With the above introduction, it is reasonable that the standard deviation of histogram, the high frequency component from 2D FFT, and the curvature in space domain are the three features that can be used for damages detection.

4.3 Reflectivity Damage Detection Process

LiDAR reflectivity defect detection can be divided into five correlative processes. Figure 4.7 demonstrates the pre-processing of the selected LiDAR data, filtration of noise within the data, division of image information into blocks for separate image processing, and the identification of the defective areas.

The Process of Reflectivity Damage Detection

LiDAR Data → Reflectivity Matrix → Filter → Sub Matrix Division → Histogram Features / 2D FFT Features / Space Curvature → Data Clustering
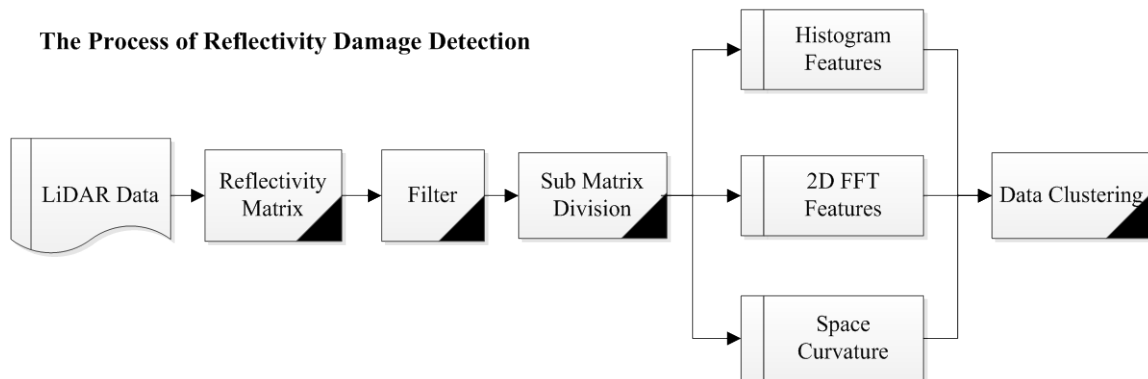
Figure 4.7 Process of the damage detection algorithm using reflectivity

4.4 Case Study

To validate the effectiveness of the algorithm, the following experiment was carried out on the Tryon Steel Bridge in Charlotte uptown area, and the bridge has rebar exposure under the deck that is clearly shown in Figure 4.8. This is a typical damage in

the curved surfaces. The reflectivity damage detection algorithm, as described in previous section, will be used to recognize the defective areas.
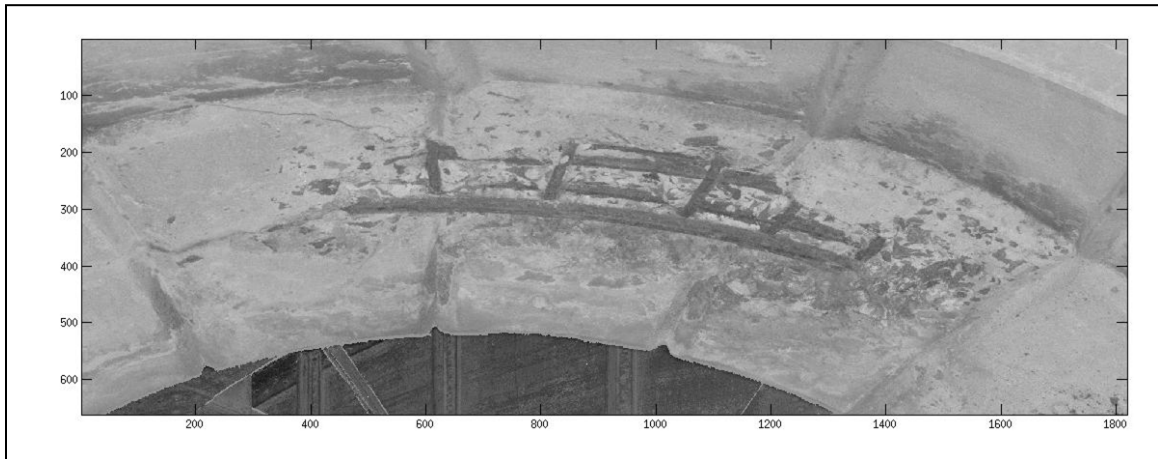
Figure 4.8 Tryon bridge with rebar exposure damage in the arc

- Decomposition

The algorithm will first import the cloud point data of the studied area and divide them into small grids (128*128) according to the column and row numbers, which is the index of the new data structure of intensity and coordinate values in the identification algorithm.

- Spatial Curvature Index

Calculate the curvature index C_{cur} of the divide girds. In Figure 4.9, it is clearly that the curvature indexes for sub grids from 58 to 66 are extremely high, and they are actually intersections between bridge structure and the background. These curvature indexes will not be included in the clustering algorithms. It is hardly to tell the variance of C_{cur} among other grids, because the intersection grids magnify the overall scale.
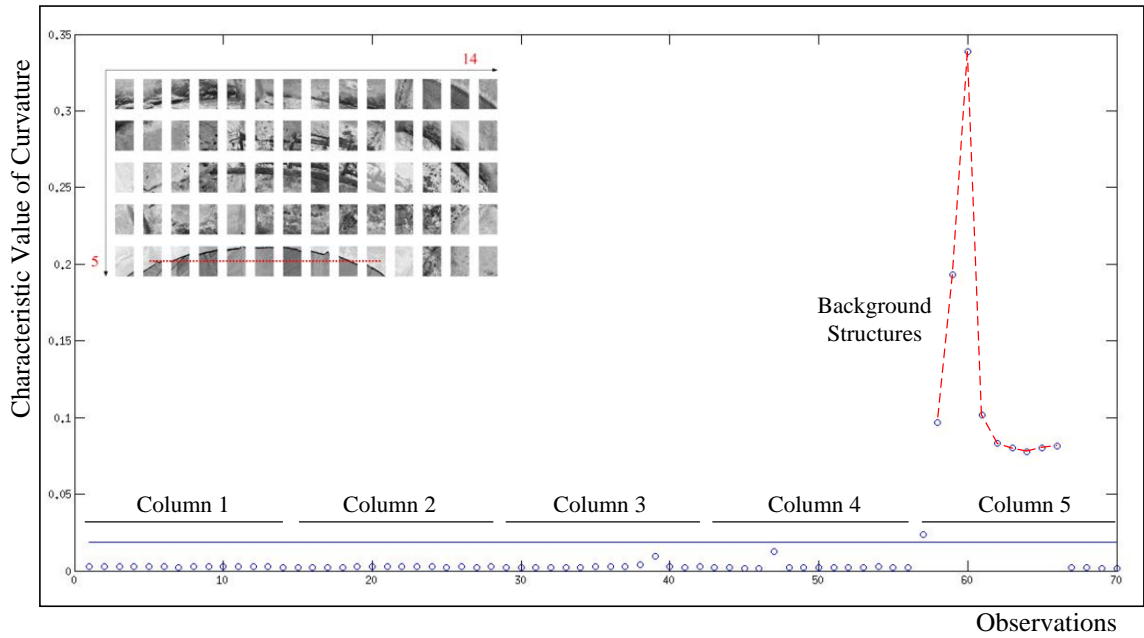
Figure 4.9 The curvature feature of the 70 divided grids

- Calculate C_{std}.

The histograms of the sub intensity matrixes are constructed in the Figure 4.10 and the standard deviation of values in the matrixes are also calculated to get the expression of the feature for intensity distribution (Figure 4.11). The distribution of the standard deviation values indicated that there are many grids that have dispersion of reflectance values.
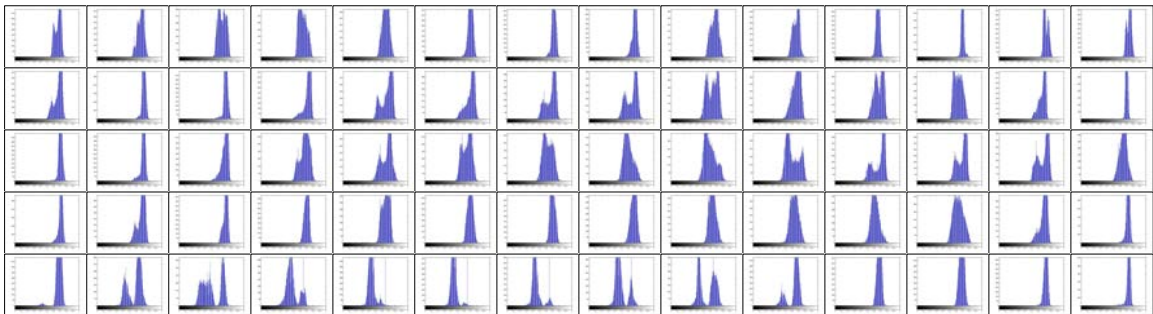
Figure 4.10 Histograms of the sub intensity matrixes
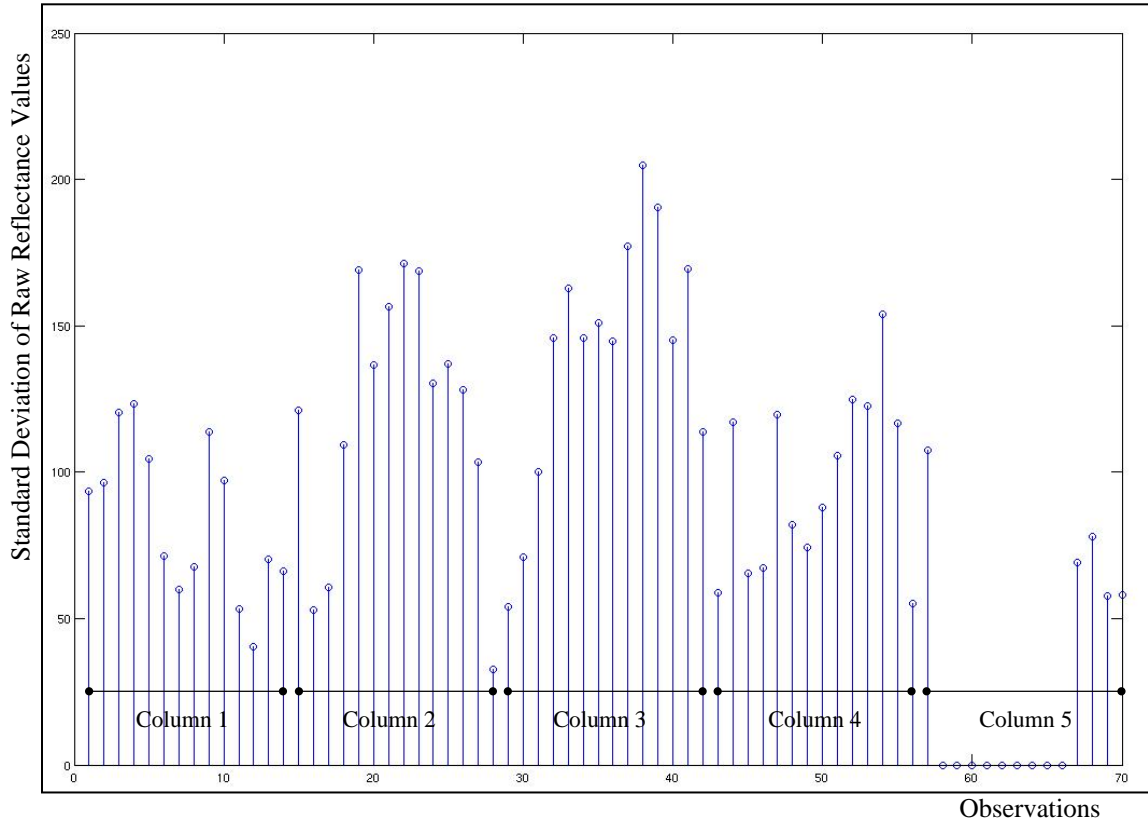
Figure 4.11 Standard deviation of raw reflectance values of observations

- Calculate $\overline{C_{fft}}$.

The $\overline{C_{fft}}$ values of the divided sub intensity matrixes are calculated to add the expression of high frequency components. A circle with the radius of 32 pixels is removed from the FFT magnitude image matrix when calculating the C_{fft}. The distribution of the $\overline{C_{fft}}$ values also indicates that many divided grids have large amount of high frequency components.
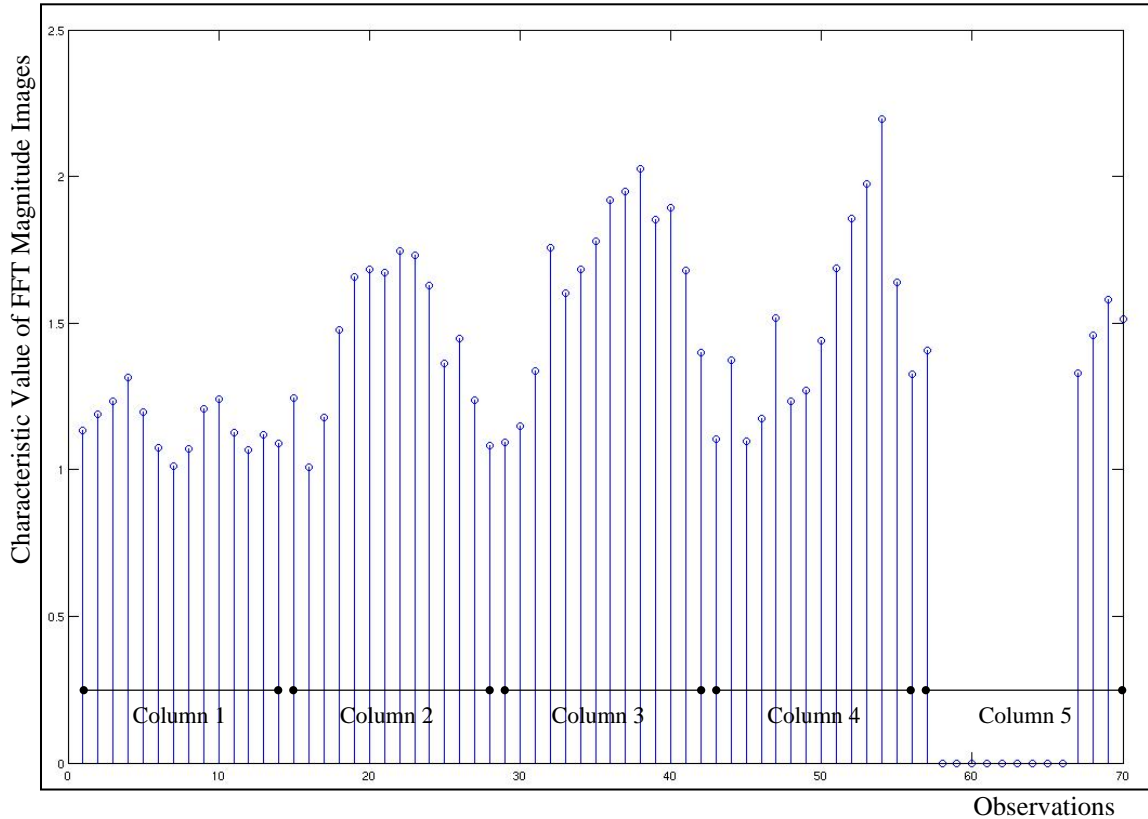
Figure 4.12 Characteristic values of the FFT magnitude image of observations

- K-Means Clustering.

In multivariate statistics, clustering is an effective method in grouping the data according to their attributes (Johnson & Wincher, 1998). The principle of clustering is individuals from the same class always are similar with each other, but individuals from different classes will show their difference.

K-Means clustering grouping is done by minimizing the sum of squares of distances between data and the corresponding cluster Centroid. The K-means clustering process can partition n dimensional (attributes) population into k subsets. The previous part of this damage detection algorithm has already provided 70 sets of data, and each of them has three attribute values: C_{std}, $\overline{C_{fft}}$, and C_{cur}. The K-means clustering algorithm is used to partition the 61 (excluding section 58 to 66) into 2 subsets, which is represented as:

$$S = \{S_1, S_2\} \tag{4-6}$$

The defective areas have been clustered together into the group with the attribute value 2, and the normal partitions are clustered into the group with the attribute value as 1. The group of data with the attribute value as zero stands for those intersection areas that have been filtered at the beginning of this damage detection algorithm.
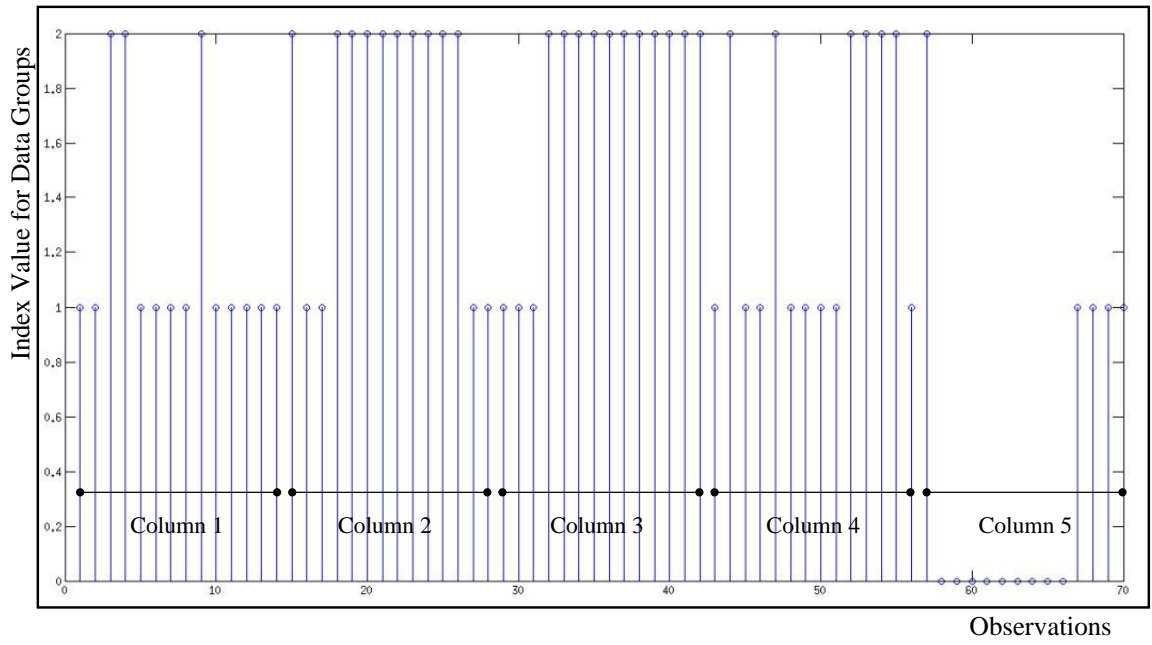
Figure 4.13 Data clustering result using three features

Figure 4.14 is the representation of the result using reflectivity algorithms in damage detection for the Tryon Steel Bridge. According to the clustering result in Figure 4.13, the sub regions marked with red dots are the damage areas recognized correctly, those with white dots are the good areas that misrecognized as defective, and one with black dot is the unrecognized damage area.
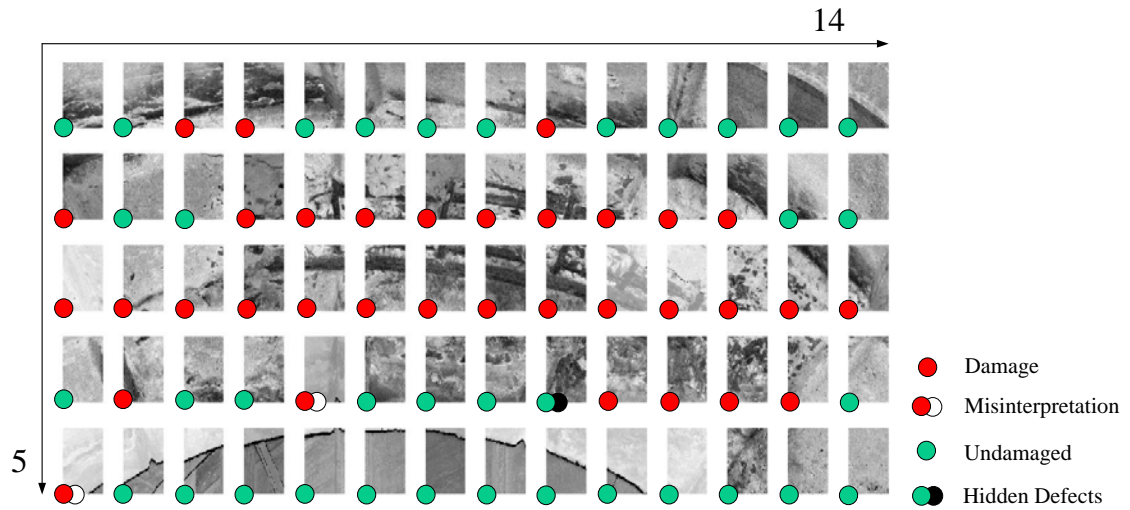
Figure 4.14 Result of the analysis using reflectivity in damage detection

One of the two grids that have been misrecognized as defective area is located in the intersection. It survived in the curvature index filter process because there is only a little portion of background points contained in this grid, thus make its C_{mn} value not as large as those filtered in the first step. The patterns of the intensity value distribution and the FFT magnitude image are similar to that of normal surfaces.

4.5 Conclusion

Restricted by the algorithm used to reconstruct 3D shape from the bridge surface damage scan data, the previous LiDAR damage detection algorithms is incapable of identifying damage in complex-shaped surfaces. In this study, an attempt is made to apply reflectance value of LiDAR data to develop enhanced automatic surface damage recognition algorithm for bridge inspection. The experiment shows the selected features and their expression is effective in damage detection. The K-Means clustering is used to group the sub grids into different classes according to the minimum distance to the Centroids.

CHAPTER 5: DECK JOINT EVALUATION AND SOIL SLOPE EVALUATION

5.1 Bridge Deck Joint Evaluation

Deck joint is an important component of highway bridges. Any cost-effective evaluation method that can help trace joint movements during frequent inspections will provide valuable data to bridge engineers. To ensure the application of remote sensing in highway bridge inspection, terrestrial LiDAR technology and aerial photography are being investigated as the proposed joint evaluation approaches. As mentioned in previous chapters, the laser scanner is able to record 3D coordination information of bridge surface points, and generate high density point cloud data for deck joints evaluation, while aerial imagery taken by commercial DSLR cameras in a small airplane flying at 1000 feet can get high resolution imagery for bridge surface components (Chen et al., 2011).

5.1.1 Bridge Deck Joint Maintenance

Deck joint is critical to the overall performance of a bridge structure, and the deck joint failures can be result from factors such as the joint material aging, improper design and installation, insufficient maintenance, excessive usage and loadings. According to the BJA (2003), the performance requirements of a joint can be classified into the following three categories:

- Structural Stability.

Bridge deck joint should be able to withstand the traffic load, and accommodate to the bridge movements arising from environmental impacts. Moreover, dynamic

 loading from sudden stresses (nature disasters) also needs to be considered in the joint design and installation.

- User Satisfactory.

The joint should provide standard experience to the road users. It has to be comfortable such as maintaining a low-level noise and vibration when driving through.

- Easy Maintenance:

The joint should be easy for maintenance, it would be better if the service will not interrupt the traffic, and the wearing elements should be easily replaceable.

The shape of the joint component and the common defects in bridge surface are important visual factors that can be used in the reorganization and identification of bridge deck joints evaluation. This study is mainly targeted at determining the sensing resolution and detection capability of the remote sensing technology, but not the severity of the joints.

In current visual dominated bridge inspection, joint inspection often requires temporarily disable of ongoing traffic, which result in inconvenience and other losses. The Spatially-Integrated Small Format Aerial Photography (SI-SFAP) has been developed to provide higher resolution images than most commercial satellites and large or medium mapping grade aerial imaging in bridge inspection (Chen et al., 2011). The two dimensional imagery can provide bridge inspectors sufficient information for the evaluation of bridge decks and parapets.

5.1.2 Bridge Deck Joint Evaluation Using LiDAR

A LiDAR scan test was conducted on the surface of the Mallard Creek Bridge, Charlotte, North Carolina. The test focuses on the deterioration area located at one of the

expansion joints. The damage along the surface can be seen in Figure 5.1. The damage selected is a typical mass loss of material from bridge deck joint component. In this particular case, the damage is seen to spread from the deck joint. The damage is quantified as 1.650-E01 m^2 for surface area and 1.583-E03 m^3 for volume.
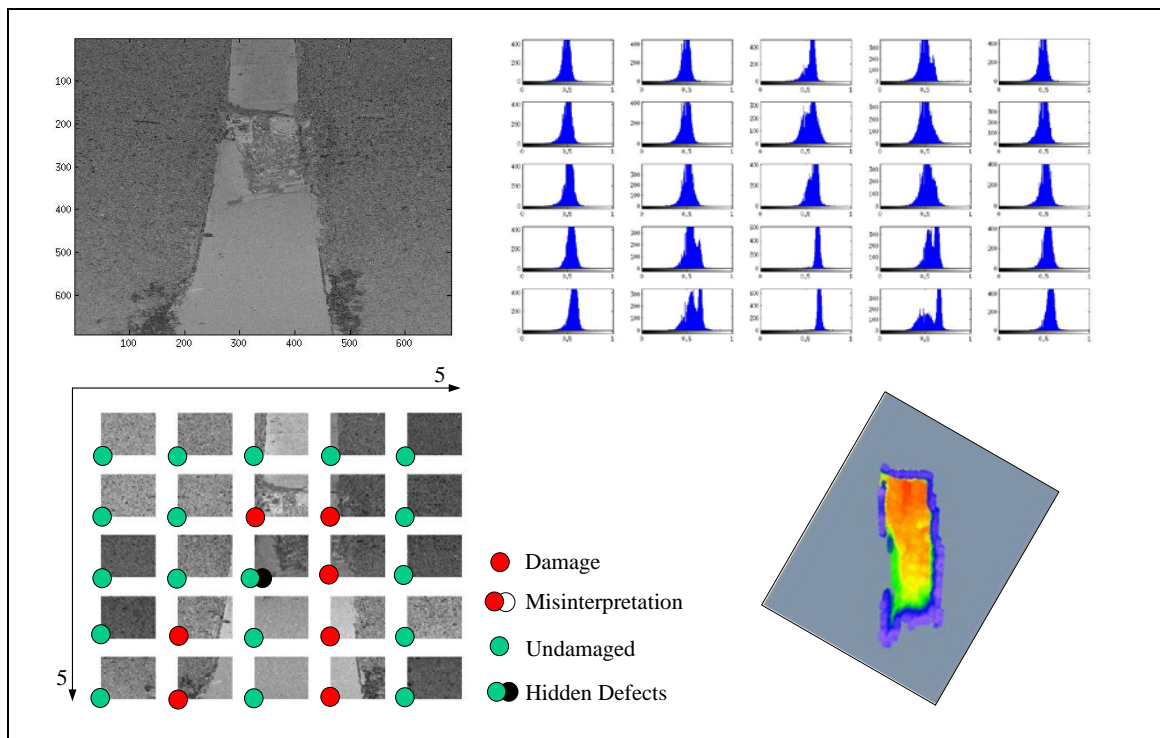
Figure 5.1 LiDAR bridge deck joint evaluation

The purpose of edge detection in bridge deck joint evaluation is to significantly reduce the amount of data in the point cloud, which is the source for the construction of 3D virtual model. John F. Canny (1967) presented a method to determine the edges in the image, which becomes the most popular one edge detection. The following is detailed procedures:

- Noise Filtering.

The image converted from LiDAR scanning data will contain noise, the Canny calculator suggests a Gaussian filter to remove noises prior the edge detection.

- Gradient Calculation.

The gradients of the image are computed to measure its change of grayscale intensity, and gradients are determined by applying 'Sobel-operator'. The magnitude of the gradient can be calculated as:

$$G = \sqrt{G_x^2(x,y) + G_y^2(x,y)} \qquad (5\text{-}1)$$

and then direction of the edges is determined by using:

$$\theta = \arctan(\frac{G_x(x,y)}{G_y(x,y)}) \qquad (5\text{-}2)$$

- Non-Maximum Suppression.

The Canny algorithm basically finds edges where the gray scale intensity of the image that changes the most. This suppression keeps all local maxima in the gradient image and deletes the rest.

- Hysteresis Thresholding.

The thresholding is set to remove noises that recognized as edge in the last three steps, which is an arbitrary value requires human interaction.

The bridge deck joint usually has a sharp edge in the inspection images. From the inspection image, human vision can easily tell where the deck joint is, and estimate its dimension as well. The image processing techniques using edge detector is also able to find the edges in a picture. The following experiment is designed to use Canny edge detector in the determining of bridge deck joint edge using LiDAR reflectance data.
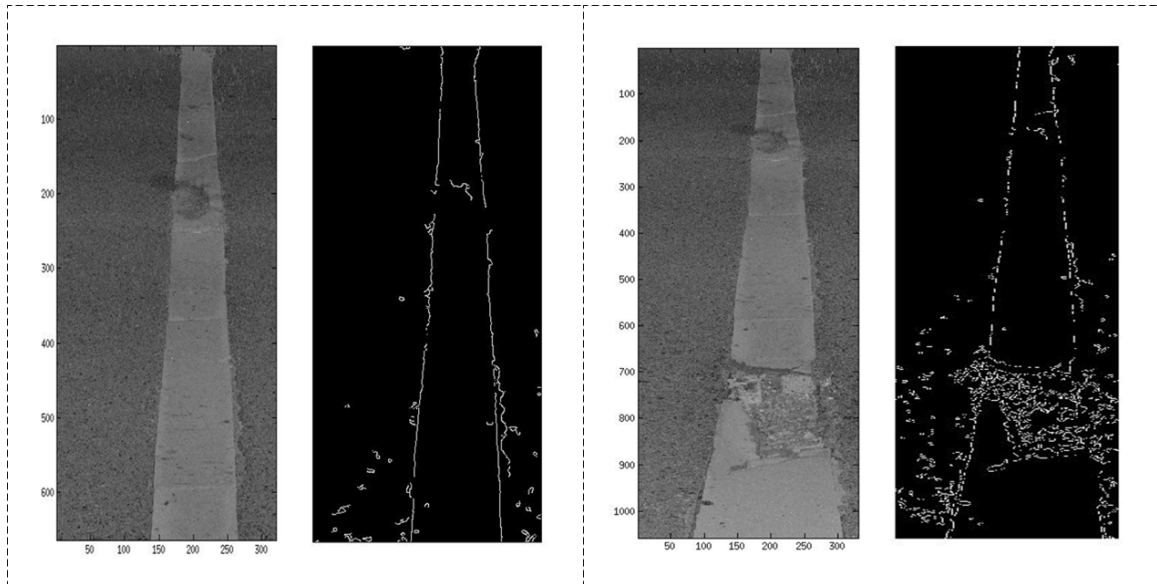
Figure 5.2 Edge detection using Canny calculator

It is clear from the above picture that the joint edge of the Mallard Creek Bridge can be well recognized using Canny algorithm for the bridge deck without damage. The result is not so good when using Canny calculator in determining the edge from the image contains large portion of defects, this is because the Canny edge detection determines the edge boundary through the magnitude, the pixel gradient, and most of the defective area images have scattering effect of the laser light, thus the gradients of those pixels are also greater than the smooth surfaces.

The quantification of expansion joints is useful in the bridge inspection, especially when the bridge joint data could be record periodically using LiDAR scanner. This will provide the bridge inspectors a convenient way to observe the joint movements. The joint dimension (width) measurements are performed for the Mallard Creek Bridge center joint. Multiple-time measurements were conducted in the test and the average value of these measurements is calculated for later comparison with the results from aerial image data. A second bridge (Alabama) was also selected in quantifying deck joint dimension

using LiDAR scan data. The Alabama bridge is a 5 span concrete highway bridge, and has good deck joint condition.

Figure 5.3 The 3D overview of Alabama bridge 10357

In order to capture three deck joints, separate scans were performed on the bridge by setting the LiDAR on the road shoulders. The first scan of the Alabama bridge was conducted near the center joint of the bridge from the shoulder, which present a good view of the interested expansion joint. The second LiDAR scan of the joint was conducted on the north part of the bridge. It is also a well captured LiDAR scan result. The third scan of the bridge was conducted in the southern part of the bridge.

5.1.3 Bridge Deck Joint Evaluation Using Aerial Imagery

The quantification capability of bridge deck joints and other kind of damage are mainly restricted by the resolution of the remote imaging technique. For the aerial imaging, a DSLR camera is mounted beneath an airplane (Cessna C210L). The Cessna was set at the cruise power setting (approx. 160 mph at 17 gph). The resolution of the digital images is defined as the ratio of the actual physical dimension to the physical length of the object in photo.

All image processing is performed in ArcGIS including the measurement of the joint dimension. By matching these points on the aerial photo to the corresponding points on a base image, each point on that aerial photo was essentially assigned a geographic coordinate, which is called georeferencing. A shapefile will be created to extract the data for the measurement after the image is georeferenced. The shapefile is also added to the viewing space in the ArcGIS software once it is generated.

For joint width measurements, a measuring line could be drawn from one side of the joint to the other using the shapefile. Since the images that are drawing on have a synchronized geographic location, the line will have a beginning coordinate and an ending coordinate. As a result, the distance of the two points can be calculated using ArcGIS. The result is a measurement with a theoretical resolution of about 0.0125m (sub inch).

The application of deck joint evaluation using aerial imagery and ArcGIS are also applied on the same bridges (Mallard Creek Bridge and Alabama Bridge). Figure 5.4 shows the aerial image taken by commercial DSLR cameras in a small plane flying at 1000 feet for the Mallard Creek Bridge deck surface. The resolution of the photograph is highly dependent on the airplane operation condition, which is typically about 0.0125 m (half of an inch).

Figure 5.4 Mallard Creek bridge joint width quantification using aerial imagery

The joint evaluation is also conducted for the second bridge located in Alabama. Figure 5.5 is the first aerial image for the center join of the bridge 10357. The pixel resolution is sub-inch and qualified for the deck joint width measurement according the bridge inspection manual.

One of the difficulties in analyzing bridge surface conditions using aerial imaging is when encountering heavily shadowed situations as shown in Figure 5.6, where the object to be measured is covered by the shadow of vegetables. In this case, it is hard to distinguish the boundaries of the joints or other surface issues. Several filter algorithms are needed to preprocess the image to reduce the shadow effect. Other than the center and south joints, Figure 5.6 shows the north joint and Figure 5.7 shows the south joint, there

are only three sample data collected for the north joint. Table 5.1 summarized the width measured using LiDAR and aerial imagery.
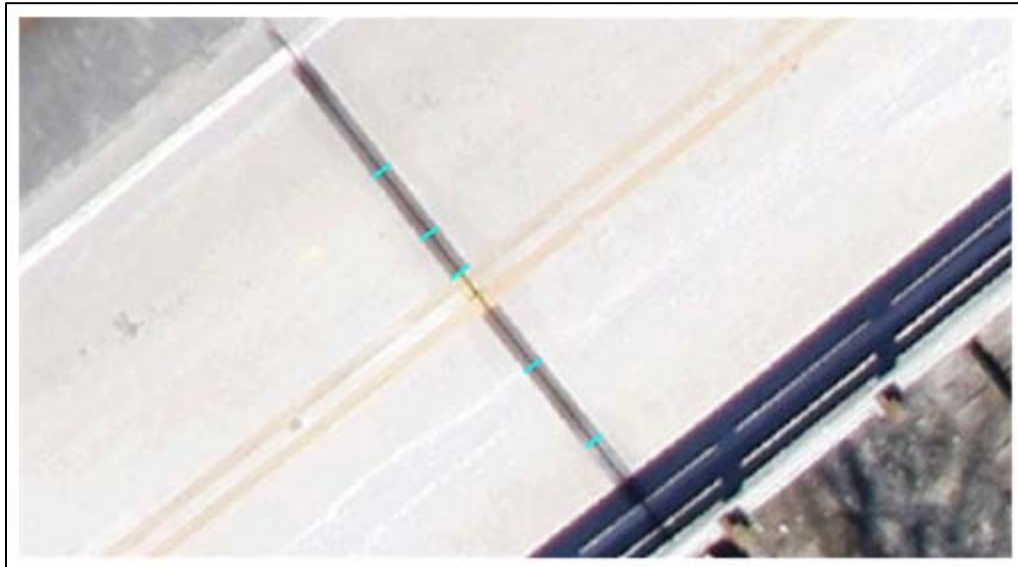
Figure 5.5 Bridge 10357 center joint width quantification using aerial imagery
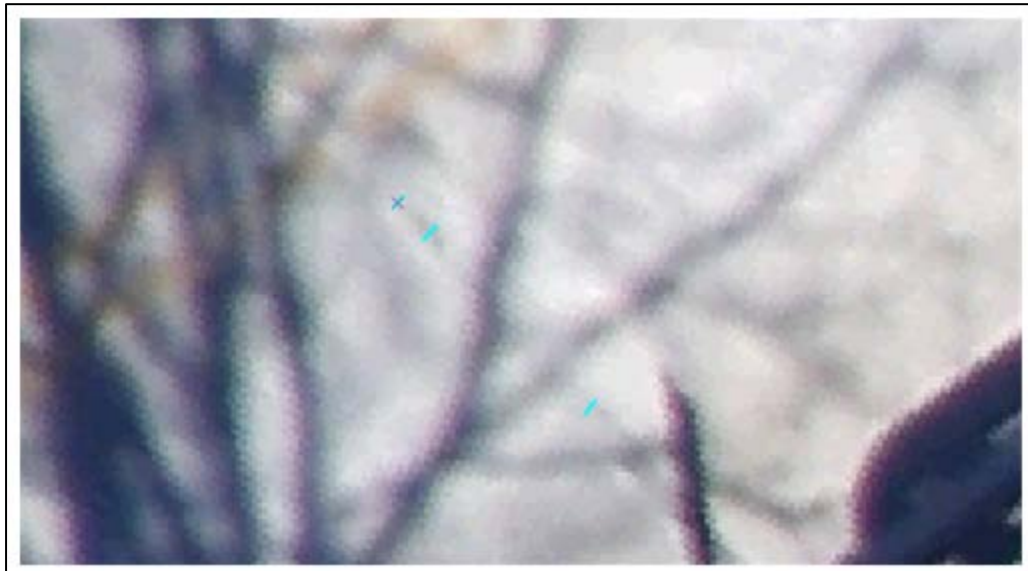
Figure 5.6 Bridge 10357 north joint width quantification using aerial imagery
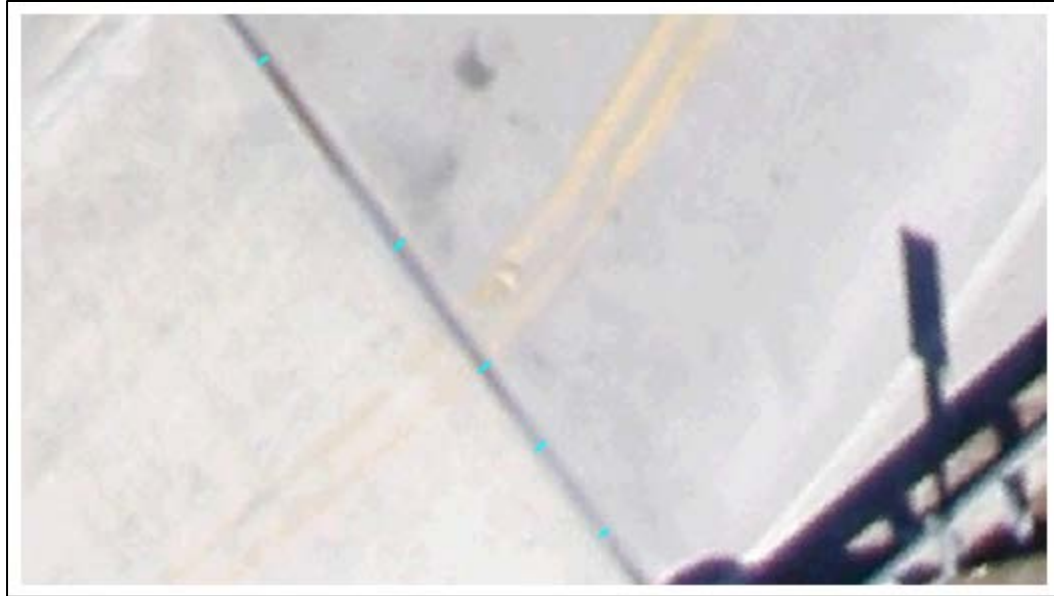
Figure 5.7 Bridge 10357 south joint width quantification using aerial imagery

Table 5.1 Width measurement of joints using LiDAR and aerial imagery

Joint Width	Mallard Creek	10357 Center	10357 North	10357 South
LiDAR	0.270m	0.226m	0.138m	0.104m
Aerial Imagery	0.354m	0.219m	0.076m	0.092m
Deviation	31.1%	3.1%	45.1%	11.5%

The results indicate that the two methods are very close in the quantitative values. Except for the north side joint of the second bridge, almost all of the joints studied using both techniques resulted in acceptable variation. As mentioned earlier, the heavy shadowing at the North Joint has resulted in less reliable data from the aerial images. Figure 5.8 summarized all the images analyzed for this study from both bridges.
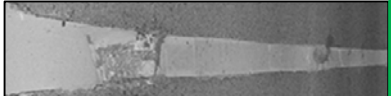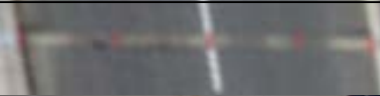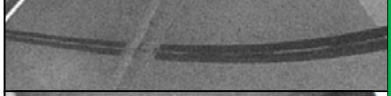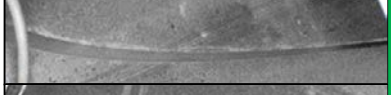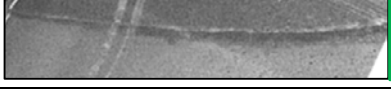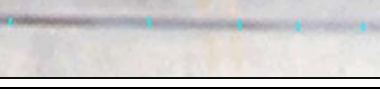
ITEMS	(a) LiDAR Scanning Data	(b) Aerial Imagery	Result
Mallard Creek Bridge Joint			(a) 0.270m (b) 0.354m
Alabama Bridge Center Joint			(a) 0.226m (b) 0.219m
Alabama Bridge North Joint			(a) 0.138m (b) 0.076m
Alabama Bridge South Joint			(a) 0.104m (b) 0.092m

Figure 5.8 Joint width quantification using LiDAR and aerial imagery

5.2 Slope Stability Study

Rain fall effects on soil erosion have been reported as early as 1895 by Wiesner. Ellison (1945) described erosion due to rainfall was carried out by three mechanisms: 1) loss of soil through surface runoffs; 2) loss of soil through raindrop splash; 3) erosional activities due to soil flow. Al-Durrah and Bradford (1982) concluded that rain drops do not compact soil by compression, but rather by breakdown of soil aggregates and packing of splashed soil. Soil erosion on unprotected bridge embankment can have devastating effects. This is especially true for mountain areas where landslides and slope failure can erode bridge foundation.
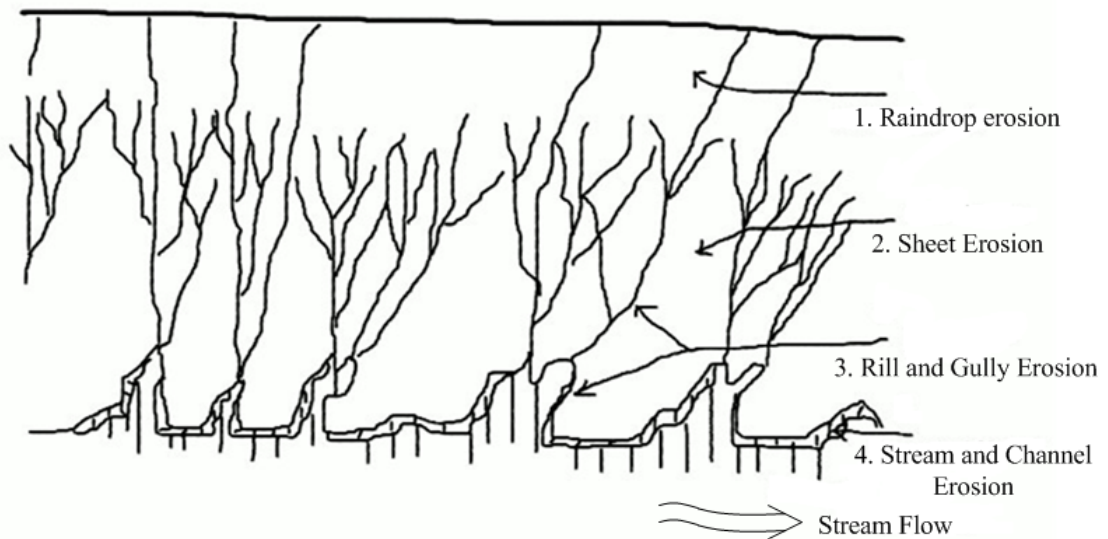
Figure 5.9 Rain erosion process on an soil slope

Rain effects on soil surface can be summarized in two aspects: 1) detachability and 2) transportability: After initial impact, the water may form a surface water film, which is affected by the detachability and not transportability. Hence, there are two possible mechanisms for reducing rain-induced erosion: 1) to form resistance against raindrop impact and 2) to form strong bonding to the ash to resist transport mechanisms. Figure 5.9 shows a graphic rendering of a rain erosion process on an soil slope, which typically involves three mechanisms: 1) raindrop erosion, 2) sheet erosion and 3) rill and gully erosion.

In this study, the rainfall effects on earth slope with homogeneous fine grained materials (simulated using fine coal ash particles) are captured using a small-scale erosion test device. Showed in Figure 5.10 is a schematic drawing of the erosion apparatus used in the small-scale erosion tests. The device consists of a spigot head, tilting ash tray and a particle collection tray. The spigot head is designed to allow dripping of water uniformly along a line. The figure also shows the actual setup

assembly including three tests where the spigot head is actually a perforated pipe with water supplied from a clear water tank. The elevated water tanks and the perforated pipe simulate rain drop process (33 cm above the ash tray base), which resembles a falling head conductivity test. No measures of the actual water drop velocity and size have been made.
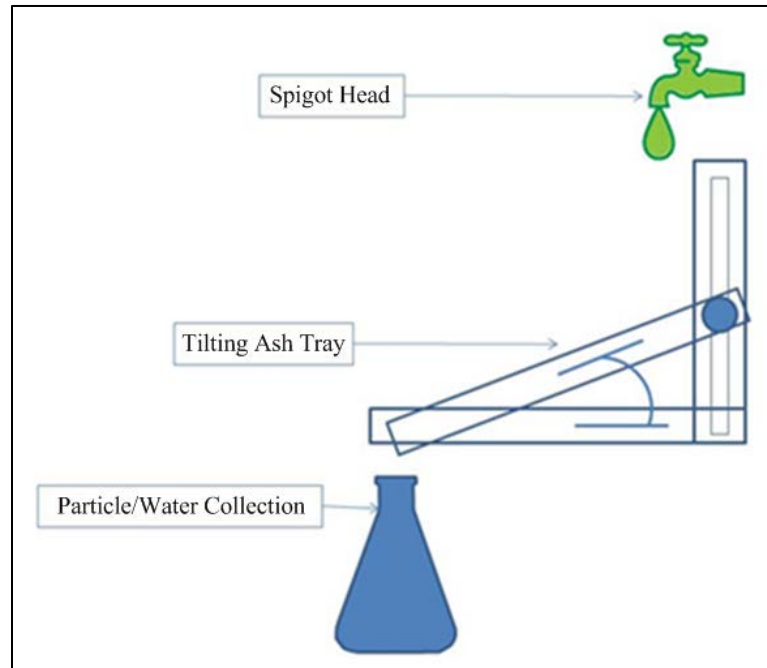
Figure 5.10 Schematic drawing of small-scale erosion test apparatus

Figure 5.11 Small-scale erosion test preparation

The coal ash is compacted into the tilt-able Plexiglas tray (30 cm length $\times$ 23.5 cm width $\times$ 4 cm depth).   Figure 5.11 shows the side view of the experimental setups. The slope of the ash tray can be altered for different slope angles up to 30 degrees. For this study, a 15 degree angle is maintained resulting in a 29 cm drop height for the rainfall simulator. Figure 5.12 shows the compacted ash sample prior to the rain erosion test. The water reservoir is filled with 500ml water and is allowed to free-fall on the ash slope simulating rainfall impact. The laser is then set in front of the test setup and conducts a full scan.
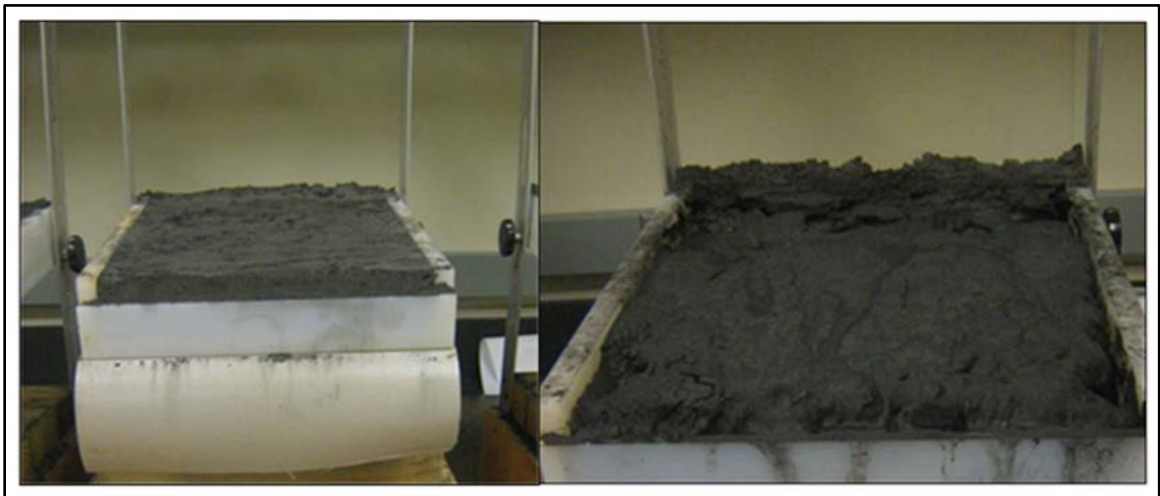
Figure 5.12 Ash sample prior to and after rain erosion test

The use of 3D laser scanner allows the volumetric quantification of the eroded slope. 3D laser scanners have been used to quantify rock outcrops (Bellian et al., 2005) and rill erosion in mine spoils (Hancock et al., 2008) Laser scan only performed on the post-rain test samples. In this study a Faro laser scanner is used and the 3D point cloud is processed using the damage quantification algorithm to determine the total mass loss (Liu et al., 2011).

Figure 5.13 shows the LiDAR scan of the four rainfall tests. The laser scanned images of the four tests performed where moderately disturbed surfaces are observed. Automated mass loss calculations are then performed on the four scans – an example calculated mass loss is shown in Figure 5.14. The right hand side image is the computed mass loss area and left hand side is the actual scan image. It is observed that the computed mass loss was divided into three large areas.
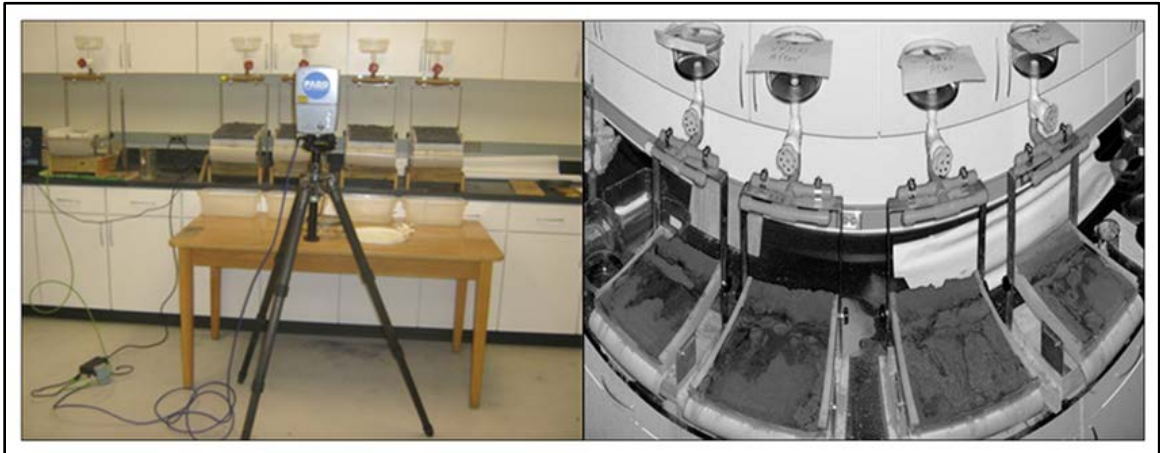
Figure 5.13 Laser scanner settlement and scanned images

The laser scanning technique has accurately quantified the mass loss due to rain erosion. However, the point cloud data point density and the reflectivity of the grey surface effect on the returning laser energy need to be further investigated. Nonetheless, this study shows great potential for the technique to be used for further quantification of mass loss on soil slopes.
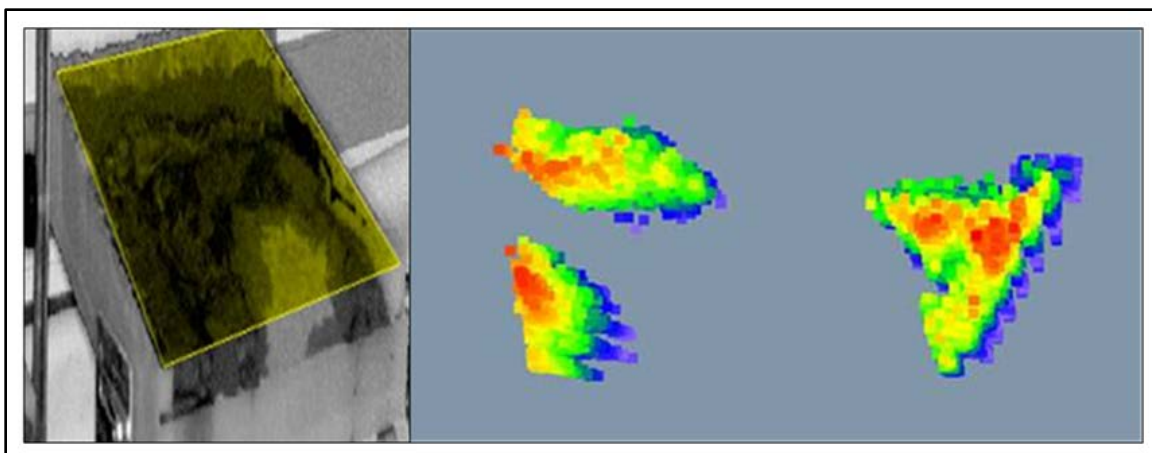
Figure 5.14 Automatic mass loss calculation showing 3 separate areas

The laboratory test setup provided a centimeter-range erosion simulation and has successfully captured the rain erosion process that would have caused mass loss during heavy rain and erode embankment slopes. 3D laser scanner was demonstrated to successfully quantify the mass loss of the rain-impact samples.

Table 5.2 The quantification of simulated slope stability study

Sample	Impacted Surfaces (m^2)	Depth Estimate (m)	Impacted Volume (m^3)
1	0.16*0.24 (3.84E-02)	1.2E-02	1.748E-04

5.3 Conclusion

In this study, the possibility of applying LiDAR scanned point cloud data and aerial imagery in bridge deck joint evaluation and slope failure is demonstrated. The Mallard Creek Bridge and the Alabama Bridge are selected and studied. The joint dimension quantification and damage detection was conducted and the results show that the LiDAR scan could be helpful for quantifying the bridge joint movements. Laboratory demonstration of rainfall on soil slope shows that laser scanner can be used to quantify slope erosion on unprotected embankments.

CHAPTER 6: QUALITY ISSUES IN LIDAR BRIDGE INSPECTION

This chapter is devoted to the discussion of the measurement errors in LiDAR scans. There are certain factors that may prevent the LiDAR from getting precise field data during bridge inspection. Coşarcă et al. (2009) studied the error sources in the terrestrial laser scanning and classify them into four categories: instrumental, object-related, environmental and methodological errors. The study indicated that '*the scan procedures should be performed with an adequate scanner*', which means the best way to avoid most of the possible errors is to select an appropriate laser for the project. The following discussion about error sources in bridge inspection is strictly related to current research.

6.1 Systematic Errors

The systematic errors are from specific laser instrument will cause an unavoidable variance in distance measurements. However, due to the high resolution of most commercial LiDAR, system error is not significant for civil structure distance measurement applications. For instance, the FARO LS880 scanner only generates 3mm errors at a 25-meter distance, which is sufficiently accurate for most of the civil engineering survey projects. Spatial resolution is not easy to define, since it is a function of the mechanical moving speed and sampling rate. Hence, point cloud recording should consider error in spatial information collection. The errors for distance measurement can

be overlapped when the point cloud data is used for the generation of virtual models in spatial.

The systematic errors also include data processing error. In the bridge inspection programs using LiDAR data, the results vary. The improvement of the LiBE damage quantification algorithm showed in Chapter 3 is one way to reduce the systematic errors in LiDAR bridge inspection.

6.2 Errors in Inspection Procedure

Systematic errors are generated during the operation of the LiDAR bridge inspection. For damage detection, the scanning angle effect. Chapter 3 indicates that to mitigate scanning angle error requires the bridge inspectors to choose the appropriate positions to perform the test. Other approach to reduce error in inspection is to avoid scanning across heavy traffic.

6.3 External Errors Sources

The most common external errors sources are environmentally introduced. For example, the change of temperature, the dust in the atmosphere, and the lighting conditions are all factors that could result in errors of the measurement.

Passing traffic effect is one of the most common issues when scanning a bridge under heavy traffic, and the vehicles allow scatters of lines in the scan, which creates trouble in the data analysis by distorting the scanned image or generate noise points in the scan data, and this issue could lead to unacceptable errors in both damage detection and clearance measurement. Figure 6.1 shows vertical lines within as scan resulted from heavy traffic crossings.
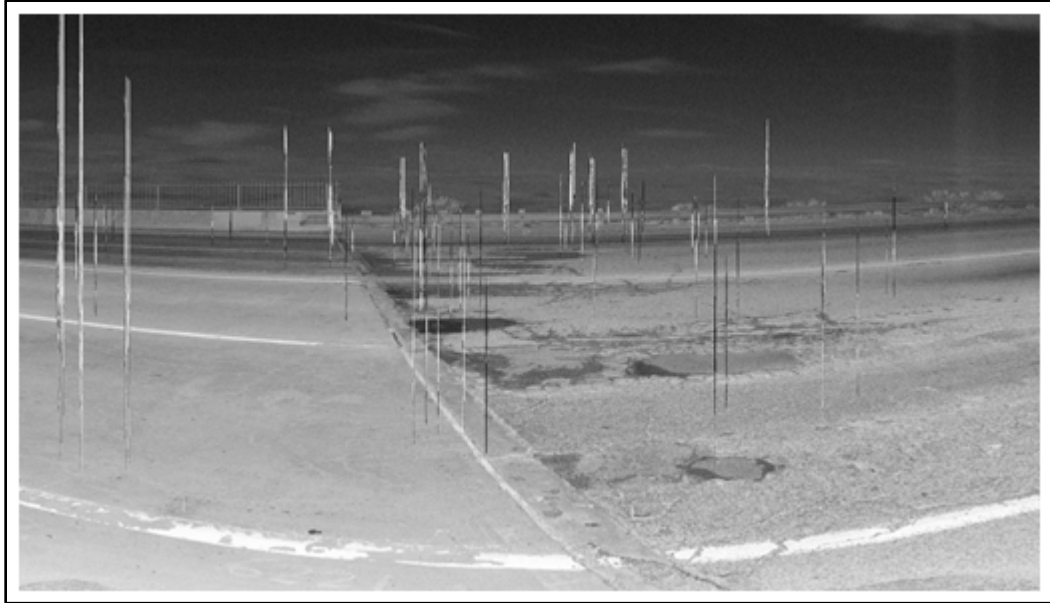
Figure 6.1 Passing traffic leaves noise in the LiDAR scan

6.3 Quality Control in LiDAR Bridge Inspection Process

Data quality control is critical and is associated with the inspection process. Quality management principles can be applied to evaluate the inspector performances, which is critical to the outcomes of inspection.

An FHWA review of existing bridge inspector performance indicates that the subjectivity involved in visual bridge inspection can introduce significant variability (Moore et al., 2001). The implementation of LiDAR into the inspection process can enhance the quality of inspection through providing quantifiable measurements of damages and critical bridge parameters, such as bridge under clearances. The following discusses specifically the LiDAR implementation for damage detection.

6.3.1 LiDAR Damage Quantification Application

One of the most advanced features of LiDAR is to quantify damage in a bridge. The quantifiable damages including defective areas such as mass loss, pot holes, or even

small damages due to concrete pop-out from corroded rebar, can be easily measured by LiDAR.

Figure 6.2 shows a large scale mass loss under a bridge girder (42300, IA). Due to the widespread damaged area, LiDAR can quantify the total damage area, which can be clearly visualized in the 3D reconstruction. The quantifiable damage can be documented and compared to future measurements.
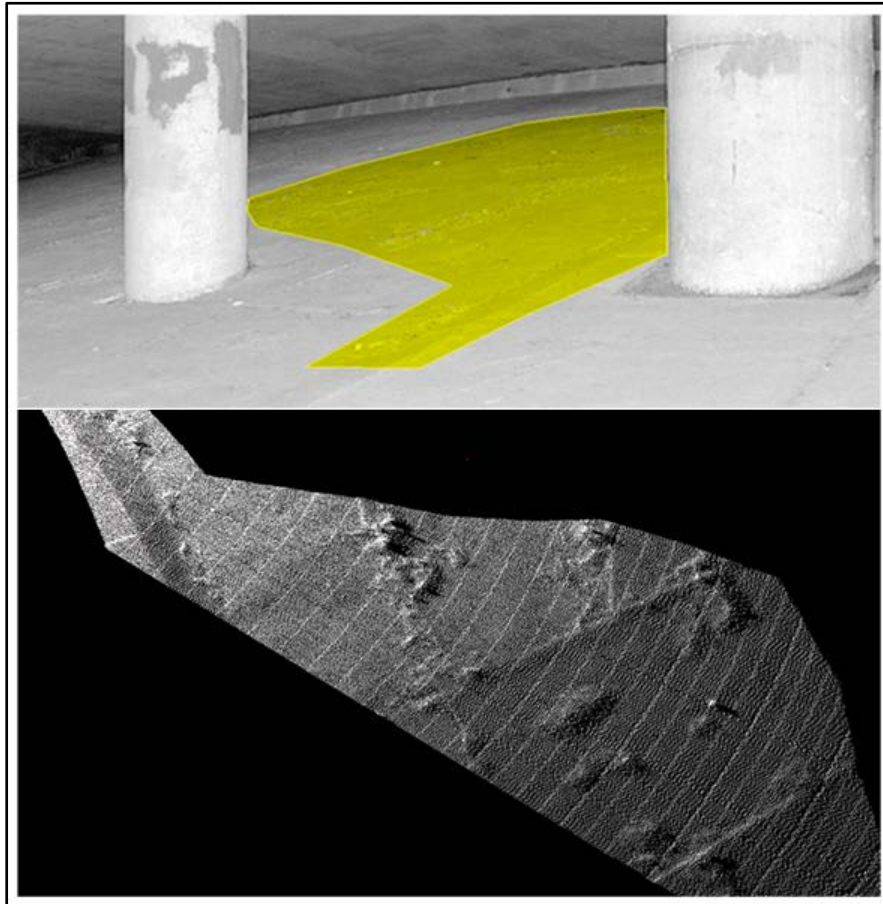
Figure 6.2 The large area bridge damage monitoring using LiDAR

Figure 6.3 shows an example of rebar damage quantification on bridge 000941 in Alabama. From the manual measurements, the length of the joint damage is 0.073m. LiBE algorithm has identified this defect successfully, and has been marked in the 3D inspection result reconstruction.
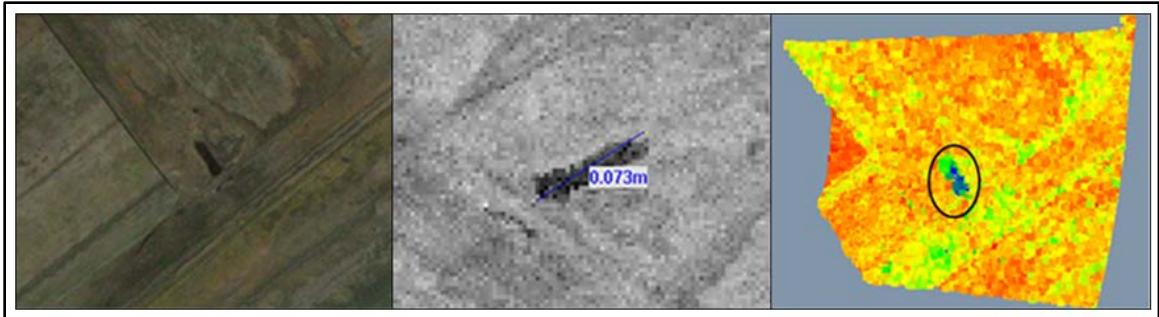
Figure 6.3 Minor rebar exposure damage in the joint

The limitation of using LiDAR for damage quantification is when the damages are too small or do not reflect enough laser points. In such cases, the inspection algorithm will not get any results.
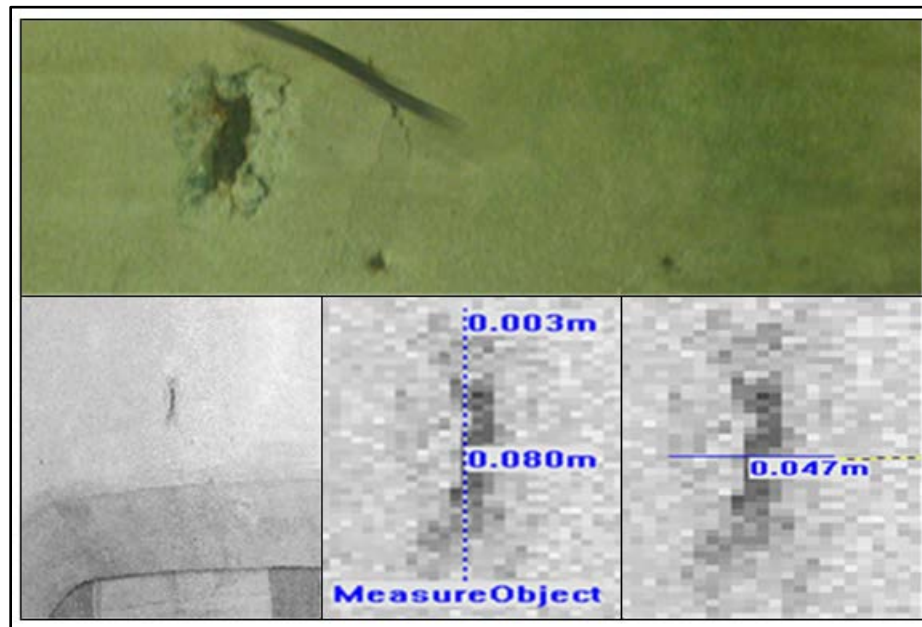
Figure 6.4 Resolution of LiDAR bridge inspection algorithms

In Figure 6.4, the damage is caused due to concrete pop-out from corroded rebars and the defect portion can be recognized on the LiDAR scan visually. The change detection algorithm failed to identify this damage due to the low pixel resolution. However, general measurement of the damage size can be determined using LiDAR scan.

The length of the damage is shown to be 0.08m with a width of 0.047m. The width is probably overestimated due to inadequate resolution.

CHAPTER 7: COMPARATIVE COST ANALYSIS

7.1 Cost Analysis

The cost analysis for LiDAR implementation is conducted to support the bridge administrations in determining the implementation potential. The quantitative analysis of various implementation alternatives in bridge management could mitigate investment risks. This analysis provides the 'big picture' estimates of the cost of LiDAR implementation during bridge inspection process versus the cost of visual inspection. The analysis can only be used as a reference and not for actual computations.

7.1.1 Problem Statement

Quality bridge condition data is critical to an effective bridge management program. The time consuming visual inspection is not able to accommodate the amount of information needed for accurate bridge condition quantification. LiDAR may be able to fill the data gap by providing critical damage quantification. Hence, the improvement of data quality from LiDAR inspection can help the allocation of limited bridge maintenance resources, which means repairing the bridge on demand.

In order to support the decision making of implementation of LiDAR bridge inspection, a comparative analysis of visual bridge inspection and LiDAR bridge inspection is conducted for Mecklenburg County, which has 368 bridges documented in the NC bridge database. The planning horizon is selected as 50 years based on the expected life span of a bridge for lifetime cost comparison.

7.2 Cost Drivers for Visual Inspection

- Average Inspection Cost per Bridge in North Carolina

The average inspection cost for each bridge is required for the calculation of the cost analysis model, however, this data set is not always accessible. The most feasible way to estimate this cost is to get the overall bridge inspection budget and the number of to be inspected bridge in this year, then the average inspection cost of a single bridge can be calculated as:

$$C = \frac{Annual\ Bridge\ Budget}{Number\ of\ to\ be\ inspected\ Bridges\ in\ this\ year} \tag{7-1}$$

According to the North Carolina State Department of Transportation's most recently bridge management information, there are 12,712 bridges across the state, and $12 million budget allocated annually for their inspection (NCDOT, 2012). In addition, the states are required to periodically inventory, inspect and rate all bridges on the public roads every two years. Thus the average annual inspection cost per bridge can be obtained by using the $12 million budget divide half of the NC bridge numbers, and it is about $1,887.98.

- The Contractor Cost

The average per bridge inspection budget can be separated into two parts: in-house review and contracting cost. The in-house review process mainly deals with the bridge inspection planning and documentation, while the contracting is the actual part of bridge inspection. Since the cost analysis is focusing on the inspection action side, the ratio of in-house vs. contracting (α) is required to calculate the actual incurred inspection cost in the site. According to Connecticut DOT (Lockhart, 2010), the state spent $50 million on bridge inspection contractors, and another 24 million on in-house reviews

from 2007 through early 2010. The in-house vs. contracting ratio is close to 0.5. Assuming North Carolina has the same distribution, the expense incurred on-site takes 67% of the total bridge inspection budget, and that is $1,887.98*67% = $1,264.95.

- Labor Cost for the Contractor

The $1,264.95 per bridge contractor cost consists of labor, material, management and contractor's profit. From several contractors' agreement for bridge inspection with New York DOT, they spend approximately 70% of their funds on the labor cost. Assuming North Carolina has the same distribution, the labor cost per bridge in 2012 is then $1,264.95*70% = $881.06. Furthermore, the bridge inspector is assumed to have a 3% annual salary increase, which means the labor cost of bridge increases in the same rate.

- The Fixed Inspection Cost

The fixed cost per bridge per inspection is the amount of money excluding the labor cost, which consists of in-house review cost, inspection material, contractor's management cost and profit, and therefore it is $1,887.98 - $881.06 = $1,006.92.

7.3 Cost Drivers for LiDAR Bridge Inspection

- LiDAR Equipment Purchase

A LiDAR scanner is required to implement the LiDAR technology into the DOT bridge inspection workflow. The current price of a qualified LiDAR scanner is approximately $60,000, and its expected life is five years, which indicates that it must be replaced with a new scanner every five years. It is assumed that purchasing one LiDAR would be adequate for the total number of bridges in Mecklenburg County. In that case,

the amount of investment to be made every five years per bridge is $60,000 \div 368 =$ $163.04.

- LiDAR Inspection Labor Cost

The cost savings from LiDAR inspection is based on its reduction of on-site inspection time compared to visual inspection. According to a study from center for automotive research of Michigan Tech (Hong et al., 2011), the DOT bridge inspection teams usually spend 4 to 6 hours for a single visual bridge inspection, which is expected to take about 30 minutes for preparation, one to five hours for inspection, and 30 minutes for data entry. Here is assumed that the average inspection time for visual bridge inspection is four hours. LiDAR bridge inspection will take 30 minutes for preparation, four different position scans (10 minutes each), off-site data analysis (25 minutes per scan), and automatic report generating (10 minutes), which brings it to a total of three hours for each bridge. Therefore, the reduced inspection time is 25%, and the labor cost for LiDAR inspection is $881.06 * 75\% = $660.79. Again, it also assumed that the labor cost will increases 3% annually.

- The Fixed Cost

The fixed cost is assumed to be same as in the visual inspection.

- Software Maintenance

The core of the LiDAR bridge inspection is the data processing software, which is estimated to be $60000 for the damage quantification and clearance algorithms development. The DOT spends approximately 21.7% of the total development cost for the maintenance and enhancement of the software in a 'Somewhat more important' level as indicated in Lientz's (1978) study. This consequent maintenance cost is evenly divided

annually in the entire project term, the annual per bridge software maintenance cost is

$60000*21.7% ÷ (368*50years) = $0.71.

- Additional Training Cost

In the Michigan Tech report, the author also pointed out that an equivalent of 10%

labor cost were spent for inspector training and support purposes, and therefore, it is

$881.06*10% = $88.11. This training cost is in the bridge inspector's lenience and

certification, and it is not included in the bridge inspection budget. The implementation

of LiDAR inspection requires additional training for the bridge inspectors. In comparing

with the 'Safety Inspection of In-Service Bridges' offered by the National Highway

Institute (NHI, 2012), the extra training for LiDAR bridge inspection onsite operation and

data processing is nearly half of the credit hours required by the visual inspection. This

training cost is assumed to occur every five years, which is the same as the useful life of a

LiDAR scanner. The amount of additional training per bridge is $88.11 * 50% = $44.05.

7.4 Cost Calculation

A comparison is made between implementing the LiDAR technology and keeping

the current visual inspection, based on the cost drivers list above. To evaluate the

feasibility of application, a cost comparison has been performed for a typical visual

inspection of a bridge versus LiDAR implementation over the entire analysis period. The

present value (PV) method has been used for this evaluation as follows:

$$PV(i, N) = \sum_{t=1}^{N} \frac{C_t}{(1+i)^t} \qquad (7\text{-}2)$$

where N is the planning horizon (50 years), C_t is the cost in year t, and i is the annual

discount rate (4%). The annual discount rate is assumed to be 4% since most of the NC

DOT projects use this rate for financial analysis. Since budgets are determined annually,

the annual worth of both alternatives have also been computed to compare overall annual

cost of each option. The annual worth (AW) of the project can be calculated using:

$$AW = PV \left[\frac{i(1+i)^N}{(1+i)^N - 1} \right] \tag{7-3}$$

where N is the planning horizon (50 years), i is the discount rate (4%).

Appendix B includes a detailed explanation of the annual cash flows of each alternative.

Excel has been used for the computations. The table below shows the results of the

comparative cost analysis

Table 7.1 Cost analysis for visual and LiDAR inspection in 50 years

Inspection	Item	50 year-total cost per bridge in Mecklenburg	50 year-total cost for the entire number of bridges in Mecklenburg
Visual	PV_{visual}	$55,386.77	$10,191,165.04
	AW_{visual}	$2,578.27	$474,400.78
LiDAR	PV_{LiDAR}	$47,962.31	$8,825,064.86
	AW_{LiDAR}	$2,232.66	$410,808.54

7.5 Conclusion

This study includes a simple cost comparison of visual inspection and LiDAR

inspection on the lifetime of a typical bridge. The result show that LiDAR

implementation is expected to cost lower than visual inspection as LiDAR could save the

county $PV_{visual} - PV_{LiDAR} = \$7,424.41$ per bridge over 50 years or $AW_{visual} - AW_{LiDAR} =$

$345.61 per bridge annually. And, over the planning horizon, LiDAR could save the

county $PV_{visual} - PV_{LiDAR} = \$1,366,091$ over 50 years for 368 bridges, or $AW_{visual} -$

$AW_{LiDAR} = \$63,592$ annually for 368 bridges.

More detailed financial analysis could include the quantification of benefits and a

cost benefit analysis and payback period analysis of each option.

CHAPTER 8: CONCLUSIONS

Terrestrial LIDAR is proposed for bridge inspection in this dissertation. The previous inspection algorithms developed by Liu (2010) is based solely on the spatial information from the point cloud data. As a continuation of the previous study, project initiated in 2007, the objective of this research is to enhance the performance from previous development by investigating ways to improve LiDAR damage detection.

The study conducted in this dissertation further verified the potential of applying LiDAR data in bridge damage inspection, and suggested several ways to improve the methodology:

(1) Revise the previous damage quantification algorithm using Delaunay Triangulation to link the scattered laser scan points in 3D space. The experiment and case study to quantify damages in real bridge both indicated improvement to the change evaluation results.

(2) The new approach to identify damages on curved surfaces where previous algorithm is incapable for has been developed using the reflectivity attribute of the laser scan data. Three features from the laser scan data are used to determine whether the studied area is actually defective.

(3) The developed inspection method has been used in new applications that should consider in bridge inspection: The bridge deck joint movement study indicated that LiDAR technology is able to determine bridge widths and can be used for temporal

study of deck joint movements. LiDAR ability to quantify slope erosion was demonstrated using laboratory rainfall method.

(4) The issues that affect inspection data quality in LiDAR bridge inspection are also studied. Data quality is so important because it made up the foundation for bridge maintenance planning. The error sources analysis from the survey technology to that in the inspection process is conducted to give out suggestions for maintaining a high quality inspection results. Detailed study on scanning angle has explicitly indicated the potential effects on quantifying area and volume of damage.

(5) The comparative cost analysis is conduct as a support to the decision making for implementing LiDAR technology into the bridge inspection workflow. The initial investment of the technology development and validation is costly as most of the cases in developing new solutions to beat the bottleneck. Considering about the labor reduction and the improvement of data quality resulted from the LiDAR technology implementation, the cost savings can be achieved in near term.

CHAPTER 9: RECOMMENDATIONS FOR FUTURE STUDY

The LiDAR bridge inspection technology discussed in this dissertation advanced previous efforts to quantify bridge surface damages with accurate and is able to detect the defective areas on curved surfaces. Several new studies can be performed benefit from the large number of bridge scans collected in this research.

Of interest is when the laser scan returns insufficient scan points making current algorithms difficult to quantify damage. Appropriate interpolation algorithms could be helpful if the additional vectors are put into the scattered LiDAR scanning points and form continuous virtual surfaces for those objects.

Pattern recognition can be integrated with the LiDAR bridge inspection to make bridge inspection more automatic and convenient. This is especially useful for differentiating damage types, and f the bridge components can be well recognized in the beginning of inspection, specific algorithms can be specified to conduct the inspection for different components. This will make the development of data processing software more focused, and can improve the inspection result at the same time.

REFERENCES

AASHTO. (2009). White paper on bridge inspection and rating. Journal of Bridge Engineering, 14(1), 1-5.

Abdel-Qader, I., Abudayyeh, O., & Kelly, M. (2003). Analysis of edge-detection techniques for crack identification in bridges. Journal of Computing in Civil Engineering, 17(4), 255-263.

Ackermann, F. (1996). Airborne laser scanning for elevation models. Geomatics Info Magazine, 10(10), 24-25.

Al-Durrah, M. M., & Bradford, J. M. (1982). The mechanism of raindrop splash on soil surfaces. Soil Sci Soc Am J, 46(5), 1086-1090.

Alonso, S. J., Rubio, M., Martín, F., & Fernández, G. (2011). Comparing time-of-flight and phase-shift. The Survey of The Royal Pantheon in the Basilica of San Isidoro (LEÓN). 4th International Workshop 3D-ARCH, 1-9.

ASCE. (2009). Report card for America's infrastructure - bridges. American Society of Civil Engineers.

Axelsson, P. (1999). Processing of laser scanner data—algorithms and applications. ISPRS Journal of Photogrammetry and Remote Sensing, 54(2-3), 138-147.

Baltsavias, E. P. (1999). Airborne laser scanning: basic relations and formulas. ISPRS Journal of Photogrammetry and Remote Sensing, 54(2-3), 199-214.

Bellian, J. A., Kerans, C., & Jennette, D. C. (2005). Digital outcrop models: applications of terrestrial scanning LIDAR technology in stratigraphic modeling. Sedimentary Research, 75, 166-176.

BJA. (2003). Standard for mechanical expansion joints. The Bridge Joint Association, 1-25.

Boehler, W., & Marbs, A. (2002). 3D Scanning instruments. Workshop on Scanning for Cultural Heritage Recording.

Brinckerhoff, P. (1993). Bridge inspection and rehabilitation: a practical guide. Wiley(Chapter 1), 1-11.

Chan, T. H. T., Yu, L., Tam, H. Y., Ni, Y. Q., Liu, S. Y., Chung, W. H., & Cheng, L. K. (2006). Fiber Bragg grating sensors for structural health monitoring of Tsing Ma bridge: background and experimental observation. Engineering Structures, 28(5), 648-659.

Chang, P. C., Flatau, A., & Liu, S. C. (2003). Review paper: health monitoring of civil infrastructure. Structural Health Monitoring, 2(3), 257-267.

Chaudhuri, D., & Samal, A. (2008). An automatic bridge detection technique for multispectral images. IEEE Transactions on Geoscience and Remote Sensing, 46(9), 2720-2727.

Chen, S., Rice, C., Boyle, C., & Hauser, E. (2011). Small-format aerial photography for highway-bridge monitoring. Journal of Performance of Constructed Facilities, 25(2), 105-112.

Chen, S. (2010). Advances in remote sensing for bridge structural health evaluation. Seventh Structural Engineering Convention, Tamil Nadu, India, 18-28.

Coşarcă, C., Jocea, A., & Savu, A. (2009). Analysis of error sources in terrestrial laser scanning. In Proceedings International Scientific Symposium GeoCAD'09, Alba Iulia, 115-124.

Delaunay, B. (1930). Über die Darstellung der Zahlen durch die binären kubischen Formen von negativer Diskriminante. Mathematische Zeitschrift, 31(1), 1-26.

Dietrich, J. I., Inkala, M. A., & Männistö, V. J. (2005). Bridge inspection and evaluation: bridge inspection quality management. Transportation Research Record: Journal of the Transportation Research Board, 1933, 1-8.

Duong, H., Pfeifer, N., & Lindenbergh, R. (2006). Full waveform analysis: Icesat laser data for land cover classification. International Archives of Photogrammetry and Remote Sensing, 36, 1-6.

Ellison, W. (1945). Some effects if raindrops and surface-flow on soil erosion and infiltration. 26, 415-430.

Faro. (2007). Phase shift measurement and time of flight measurement. Faro Technology White Paper.

Farrar, C. R., Sohn, H., Fugate, M. L., & Czarnecki, J. J. (2001). Integrated structural health monitoring. SPIE's 8th Annual International Symposium on Smart Structures and Materials, 1-9.

FHWA. (2004). National Bridge Inspection Standards. Federal Register, 69(239).

FHWA. (2012). Traffic Volume Trends. Federal Highway Adminstration - Office of Highway Policy Information., 1-10.

Girardeau-Montauta, D., Rouxa, M., Marcb, R., & Thibaultb, G. (2005). Change detection on points cloud data acquired with a ground laser scanner. ISPRS Workshop Laser Scanning 2005.

Hancock, G. R., Crawter, D., Fityus, S. G., Chandler, J., & Wells, T. (2008). The measurement and modelling of rill erosion at angle of repose slopes in mine spoil. Earth Surface Processes and Landforms, 33(7), 1006-1020.

Haugerud, R. A., & Harding, D. J. (2001). Some algorithms for virtual deforestation (VDF) of LiDAR topographic survey data. International Archives of Photogrammetry and Remote Sensing, XXXIV-3(W4), 1-7.

He, X. D., Torrance, K. E., Sillion, F. X., & Greenberg, D. P. (1991). A comprehensive physical model for light reflection. Paper presented at the Proceedings of the 18th Annual Conference on Computer Graphics and Interactive Techniques.

Hearn, G., Purvis, R. L., & Thompson, P. (2002). Bridge maintenance and management: a look to the future. TRB - Transportation in the New Millennium, 1-7.

Hong, Q., Wallace, R., Brooks, C., Endsley, A., Forster, M., Birmingham, M., & de Meloe Silva, H. (2011). Technical assessment and economic valuation update. Center for Automotive Research of Michigan Tech, 1-32.

Imhof, D. (2005). Risk assessment of existing bridge structures. PhD Dissertation. University of Cambridge.

Karp, B., Rittel, D., & Durban, D. (2008). Health monitoring of joints using dynamic end effects. Journal of Sound and Vibration, 312(1-2), 257-272.

Ko, J. M., & Ni, Y. Q. (2005). Technology developments in structural health monitoring of large-scale bridges. Engineering Structures, 27(12), 1715-1725.

Lauzon, R. G. (2000). Automated vertical clearance measurement during photolog operations. Connecticut Department of Transportation.

Lertrattanapanich, S., & Bose, N. K. (2002). High resolution image formation from low resolution frames using Delaunay Triangulation. IEEE Transactions on Image Processing, 11(12), 1427-1441.

Li, M., Cheng, L., Gong, J., Liu, Y., Chen, Z., Li, F., Song, X. (2009). Post-earthquake assessment of building damage degree using LiDAR data and imagery. Science in China Series E: Technological Sciences, 51(S2), 133-143.

Li, Q., Zou, Q., & Liu, X. (2011). Pavement crack classification via spatial distribution features. EURASIP Journal on Advances in Signal Processing, 2011, 12.

Lientz, B. P., Swanson, E. B., & Tompins G. E. (1987). Characteristics of application software maintenance. Commun. ACM, 21(6), 466-471.

Liu, W. (2010). Terrestrial LiDAR-Based Bridge Evaluation. PhD Dissertation. UNC Charlotte.

Liu, W., Chen, S., & Hauser, E. (2011). LiDAR-based bridge structure defect detection. Experimental Techniques, 35(6), 27-34.

Liu, W., Chen, S., & Hauser, E. (2009). Remote sensing for bridge health monitoring. Atmospheric and Environmental Remote Sensing Data Processing and Utilization, 1-5.

Mass, H., & Vosselman, G. (1999). Two algorithms for extracting building model from raw laser altimetry data. ISPRS Journal of Photogrammetry and Remote Sensing, 54(2-3), 153-163.

McLinn, J. (2009). Major bridge collapses in the US, and around the world. IEEE Reliability Society 2009 Annual Technology Report, 1-5.

Moore, M., Phares, B., Graybeal, B., Rolander, D., & Washer, G. (2001). Reliability of visual inspection for highway bridges, Volume 1: Final Report. Federal Highway Administration, FHWA-RD-01-020, 516.

NCDOT. (2012). North Carolina Bridge Information. North Carolina Department of Transportation (http://www.ncdot.gov/projects/ncbridges/).

NHI. (2012). Course description: safety inspection of in-service bridges. National Highway Institute.

Oliveira, H., & Correia, P. L. (2012). Automatic road crack detection and characterization. IEEE Transactions on Intelligent Transportation Systems, PP(99), 1-14.

Orcesi, A. D., & Frangopol, D. M. (2010). Optimization of bridge management under budget constraints. Transportation Research Record, 2202(2010), 148-158.

Pfeifer, N., & Briese, C. (2007). Laser scanning - principles and applications.

Ren, W., Zhao, T., & Harik, I. (2004). Experimental and analytical modal analysis of steel arch bridge. Journal of Structural Engineering, 130(7), 1022-1031.

Ribarsky, W., Hauser, E., & Chen, S. (2009). Integrated remote sensing and visualization (IRSV) system for transportation infrastructure operations and management, Poster Presentation. Transportation Research Board Annual Meeting, Washington D.C.

Shewchuk, J. R. (1999). Lectures notes on Delaunay mesh generation. University of California at Berkeley.

Soudarissanane, S., Van Ree, J., Bucksch, A., & Lindenbergh, R. (2007). Error budget of terrestrial laser scanning: influence of the incidence angle on the scan quality. 3D-NordOst 2007, Berlin, Germany.

Subramanian, N. (2008). I-35W Mississippi River bridge failure – is it a wake up call? The Indian Concrete Journal, 19(9), 29-38.

Wagner, W., Ullrich, A., Ducic, V., Melzer, T., & Studnicka, N. (2006). Gaussian decomposition and calibration of a novel small-footprint full-waveform digitising airborne laser scanner. ISPRS Journal of Photogrammetry and Remote Sensing, 60(2), 100-112.

Wang, M. L., Heo, G., & Satpathi, D. (1997). Dynamic characterization of a long span bridge: a finite element based approach. Soil Dynamics and Earthquake Engineering, 16(7-8), 503-512.

Yan, Y., Guofu, Q., & Jinping, O. (2010). Self-powered wireless corrosion monitoring sensors and networks. Sensors Journal, IEEE, 10(12), 1901-1902.

APPENDIX A: LIDAR REFELCTIVITY DAMAGE DETECTION PROGRAM

```
%% import data
x = importdata('Point Cloud Data.txt');
y = [x(:,1)-min(x(:,1))+1,x(:,2)-
min(x(:,2))+1,x(:,3:end)];
R = mean(y(:,6))*ones(max(x(:,1))-
min(x(:,1))+1,max(x(:,2))-min(x(:,2))+1);
sizer = size(R);

for ii = 1:sizer(1)
index = find(y(:,1) == ii);
R(ii,y(index,2)) = y(index,6);
end
figure;
imagesc(R);colormap(gray);

%% Collect the curvature, i.e., the third feature
cmean
% clear all;
% close all;
% clc;

% import data
% x = importdata(Point Cloud Data.txt');
y = [x(:,1)-min(x(:,1))+1,x(:,2)-
min(x(:,2))+1,x(:,3:end)];
datax = mean(y(:,3))*ones(max(x(:,1))-
min(x(:,1))+1,max(x(:,2))-min(x(:,2))+1);
datay = mean(y(:,4))*ones(max(x(:,1))-
min(x(:,1))+1,max(x(:,2))-min(x(:,2))+1);
dataz = mean(y(:,5))*ones(max(x(:,1))-
min(x(:,1))+1,max(x(:,2))-min(x(:,2))+1);
sizedatam = size(datax);
 for ii = 1:sizedatam(1)
index = find(y(:,1) == ii);
data(ii,y(index,2)) = y(index,6);
datax(ii,y(index,2)) = y(index,3);
datay(ii,y(index,2)) = y(index,4);
dataz(ii,y(index,2)) = y(index,5);
 end
 figure;
 imagesc(data);colormap(gray);

 %% devide matrix
resolx = 128; resoly = 128;
nrow = floor(sizedatam(1)/resolx); ncol =
floor(sizedatam(2)/resoly);
c = 1;
for ir = 1:nrow
        for ic = 1:ncol
        subr{c} = data(((ir-
1)*resolx+1):ir*resolx,((ic-
1)*resoly+1):ic*resoly);
```

```
        subrx{c} = datax(((ir-
1)*resolx+1):ir*resolx,((ic-
1)*resoly+1):ic*resoly);
        subry{c} = datay(((ir-
1)*resolx+1):ir*resolx,((ic-
1)*resoly+1):ic*resoly);
        subrz{c} = dataz(((ir-
1)*resolx+1):ir*resolx,((ic-
1)*resoly+1):ic*resoly);
        c = c+1;
        end
end
figure;
c = c-1;
for i1 = 1:c
        subplot(5,14,i1)
        imagesc(subr{i1});colormap(gray);
        axis off;
end

for isubm = 1:70
        Rx = subrx{isubm}; Ry =
subry{isubm}; Rz = subrz{isubm};
s = size(Rx);
D1 = sqrt((Rx(2:end-1,2:end-1)-Rx(1:end-
2,2:end-1)).^2 + (Ry(2:end-1,2:end-1)-Ry(1:end-
2,2:end-1)).^2+ (Rz(2:end-1,2:end-1)-Rz(1:end-
2,2:end-1)).^2);
D2 = sqrt((Rx(2:end-1,2:end-1)-Rx(2:end-
1,3:end)).^2 + (Ry(2:end-1,2:end-1)-Ry(2:end-
1,3:end)).^2 + (Rz(2:end-1,2:end-1)-Rz(2:end-
1,3:end)).^2);
D3 = sqrt((Rx(2:end-1,2:end-1)-Rx(3:end,2:end-
1)).^2 + (Ry(2:end-1,2:end-1)-Ry(3:end,2:end-
1)).^2 + (Rz(2:end-1,2:end-1)-Rz(3:end,2:end-
1)).^2);
D4 = sqrt((Rx(2:end-1,2:end-1)-Rx(2:end-
1,1:end-2)).^2 + (Ry(2:end-1,2:end-1)-Ry(2:end-
1,1:end-2)).^2 + (Rz(2:end-1,2:end-1)-Rz(2:end-
1,1:end-2)).^2);

D5 = sqrt((Rx(2:end-1,2:end-1)-Rx(1:end-
2,3:end)).^2 + (Ry(2:end-1,2:end-1)-Ry(1:end-
2,3:end)).^2 + (Rz(2:end-1,2:end-1)-Rz(1:end-
2,3:end)).^2);
D6 = sqrt((Rx(2:end-1,2:end-1)-
Rx(3:end,3:end)).^2 + (Ry(2:end-1,2:end-1)-
Ry(3:end,3:end)).^2 + (Rz(2:end-1,2:end-1)-
Rz(3:end,3:end)).^2);
D7 = sqrt((Rx(2:end-1,2:end-1)-Rx(3:end,1:end-
2)).^2 + (Ry(2:end-1,2:end-1)-Ry(3:end,1:end-
2)).^2 + (Rz(2:end-1,2:end-1)-Rz(3:end,1:end-
2)).^2);
```

```
D8 = sqrt((Rx(2:end-1,2:end-1)-Rx(1:end-
2,1:end-2)).^2 + (Ry(2:end-1,2:end-1)-Ry(1:end-
2,1:end-2)).^2 + (Rz(2:end-1,2:end-1)-Rz(1:end-
2,1:end-2)).^2);

C1 = zeros(4,s(1)-2,s(2)-2);
C1(1,:,:)  = D1;
C1(2,:,:) = D2;
C1(3,:,:)  = D3;
C1(4,:,:) = D4;

C2 = zeros(4,s(1)-2,s(2)-2);
C2(1,:,:)  = D5;C2(2,:,:) = D6; C2(3,:,:)  = D7;
C2(4,:,:) = D8;
C = std(C1)+std(C2)./sqrt(2);
cmean(isubm) = mean(mean(C));
end
save cmean cmean;
figure; plot(cmean,'o');
line([1,70],[mean(cmean),mean(cmean)]);

% clear all;
% close all;
% clc;
%
%% import data
x = importdata(Point Cloud Data.txt');
y = [x(:,1)-min(x(:,1))+1,x(:,2)-
min(x(:,2))+1,x(:,3:end)];
R = mean(y(:,6))*ones(max(x(:,1))-
min(x(:,1))+1,max(x(:,2))-min(x(:,2))+1);
sizer = size(R);

 for ii = 1:sizer(1)
index = find(y(:,1) == ii);
R(ii,y(index,2)) = y(index,6);
 end
 figure;
 imagesc(R);colormap(gray);

 %% devide matrix
subr={};
nrow = 128; ncol = 128;
resoly = 5; resolx = 14;
c = 1;
for ir = 1:floor(sizer(1)/nrow)
        for ic = 1:floor(sizer(2)/ncol)
        subr{c} = R(((ir-
1)*nrow+1):ir*nrow,((ic-1)*ncol+1):ic*ncol);
        c = c+1;
        end
end
```

```
%% image of submatrix
c = c-1;
figure;
for i1 = 1:c
        subplot(5,14,i1)
        imagesc(subr{i1});colormap(gray);
        axis off;
end
%% calculate std of submatrices, plot the results
for i2 = 1:c
   submatrixstd(i2,1) = std2(subr{i2});
end
plot(submatrixstd,'o');
line([1,70],[mean(submatrixstd),mean(submatrix
std)]);
%% histogram
for i3 = 1:c
subI{i3} = mat2gray(subr{i3},[0,2047]);
end
close all;figure('name','hist');
for i4 = 1:c
        subplot(5,14,i4);
        imhist(subI{i4}) ;
end
%% FFT
for i5 = 1:c
        fftImage = fftshift(fft2(subI{i5}));
        ampImage{i5} = abs(fftImage);
%        imshow(ampImage{i5});
end
%% get rid of a circle region in the middle
submatrix
for i6 = 1:c
        indrow = repmat([1:128]',1,128);
        indcol = repmat([1:128],128,1);
        dis = (indrow-64).^2 + (indcol - 64).^2;
        ampImage{i6}(find(dis<32^2)) = 0;
        cfftsum(i6,1) =
sum(sum(ampImage{i6}));
        cfftmean(i6,1) =
mean(mean(ampImage{i6}));
end
figure;plot(cfftsum,'o');
line([0,70],[mean(cfftsum),mean(cfftsum)]);
figure;plot(cfftmean,'o');line([0,70],[mean(cfftme
an),mean(cfftmean)]);
%% classification
load('cmean.mat');
X = [submatrixstd,cfftmean,cmean'];
opts = statset('Display','final');
Y = kmeans(X,2,'Distance','sqEuclidean');
[idx,ctrs] = kmeans(X,2,'Distance','sqEuclidean');
```

APPENDIX B: COMPARATIVE COST ANALYSIS

Cost Analysis Parameters	
Factual	
Item	Amount
NC Annual Inspection	$ 12,000,000.00
Number of NC Bridges	12712
Required Inspection Interval	2 Years
The Contractor Cost in Budget	66.67%
Labor Cost for the Contractor	70.00%
Annual Labor Increase	3.00%
Mecklenburg County Bridges	368
Annual Discount Rate	4.00%
Visual Inspection	
Item	Amount
Visual Inspection Per Bridge in 2012	$ 1,887.98
Labor Cost per Bridge in 2012	$ 881.06
Fixed Cost	$ 1,006.92
Training Cost Per Bridge	$ 88.11
LiDAR Inspection	
Item	Amount
Purchase for LiDAR	$ 60,000.00
Initial Software Development	$ 60,000.00
LiDAR Labor Cost in 2012	$ 660.79
Annual Software Update	$ 0.71
Fixed Cost	$ 1,006.92
Reduced Labor	25.00%
Additional Training (5 Years)	$ 44.05
LiDAR Purchase	$ 60,000.00
LiDAR Life Cycle	5 Years
LiDAR Purchase Shared by All bridges	$ 163.04

Mecklenburg County Bridge Inspection Cost (Per Bridge Per Year)
Visual Inspection

Year	Term	Labor	The Fixed Cost	Sub Total
	0	0	0	0
2012	1	$ 881.06	$ 1,006.92	$ 1,887.98
2013	2	$ 907.49	$ 1,006.92	$ 1,914.41
2014	3	$ 934.71	$ 1,006.92	$ 1,941.64
2015	4	$ 962.76	$ 1,006.92	$ 1,969.68
2016	5	$ 991.64	$ 1,006.92	$ 1,998.56
2017	6	$ 1,021.39	$ 1,006.92	$ 2,028.31
2018	7	$ 1,052.03	$ 1,006.92	$ 2,058.95
2019	8	$ 1,083.59	$ 1,006.92	$ 2,090.51
2020	9	$ 1,116.10	$ 1,006.92	$ 2,123.02
2021	10	$ 1,149.58	$ 1,006.92	$ 2,156.50
2022	11	$ 1,184.07	$ 1,006.92	$ 2,190.99
2023	12	$ 1,219.59	$ 1,006.92	$ 2,226.51
2024	13	$ 1,256.18	$ 1,006.92	$ 2,263.10
2025	14	$ 1,293.86	$ 1,006.92	$ 2,300.78
2026	15	$ 1,332.68	$ 1,006.92	$ 2,339.60
2027	16	$ 1,372.66	$ 1,006.92	$ 2,379.58
2028	17	$ 1,413.84	$ 1,006.92	$ 2,420.76
2029	18	$ 1,456.25	$ 1,006.92	$ 2,463.18
2030	19	$ 1,499.94	$ 1,006.92	$ 2,506.86
2031	20	$ 1,544.94	$ 1,006.92	$ 2,551.86
2032	21	$ 1,591.29	$ 1,006.92	$ 2,598.21
2033	22	$ 1,639.03	$ 1,006.92	$ 2,645.95
2034	23	$ 1,688.20	$ 1,006.92	$ 2,695.12
2035	24	$ 1,738.84	$ 1,006.92	$ 2,745.77
2036	25	$ 1,791.01	$ 1,006.92	$ 2,797.93
2037	26	$ 1,844.74	$ 1,006.92	$ 2,851.66
2038	27	$ 1,900.08	$ 1,006.92	$ 2,907.00
2039	28	$ 1,957.08	$ 1,006.92	$ 2,964.01
2040	29	$ 2,015.80	$ 1,006.92	$ 3,022.72
2041	30	$ 2,076.27	$ 1,006.92	$ 3,083.19
2042	31	$ 2,138.56	$ 1,006.92	$ 3,145.48
2043	32	$ 2,202.71	$ 1,006.92	$ 3,209.64
2044	33	$ 2,268.80	$ 1,006.92	$ 3,275.72
2045	34	$ 2,336.86	$ 1,006.92	$ 3,343.78
2046	35	$ 2,406.97	$ 1,006.92	$ 3,413.89
2047	36	$ 2,479.17	$ 1,006.92	$ 3,486.10
2048	37	$ 2,553.55	$ 1,006.92	$ 3,560.47
2049	38	$ 2,630.16	$ 1,006.92	$ 3,637.08
2050	39	$ 2,709.06	$ 1,006.92	$ 3,715.98

2051	40	$ 2,790.33	$ 1,006.92	$ 3,797.25
2052	41	$ 2,874.04	$ 1,006.92	$ 3,880.96
2053	42	$ 2,960.26	$ 1,006.92	$ 3,967.19
2054	43	$ 3,049.07	$ 1,006.92	$ 4,055.99
2055	44	$ 3,140.54	$ 1,006.92	$ 4,147.47
2056	45	$ 3,234.76	$ 1,006.92	$ 4,241.68
2057	46	$ 3,331.80	$ 1,006.92	$ 4,338.73
2058	47	$ 3,431.76	$ 1,006.92	$ 4,438.68
2059	48	$ 3,534.71	$ 1,006.92	$ 4,541.63
2060	49	$ 3,640.75	$ 1,006.92	$ 4,647.67
2061	50	$ 3,749.97	$ 1,006.92	$ 4,756.90
PV		$55,386.77 (S)	$10,191,165.04 (T)	
AW		$2,578.27 (S)	$474,400.78 (T)	

Mecklenburg County Bridge Inspection Cost (Per Bridge Per Year)						
LiDAR Inspection						
Year	Term	Purchase & Training	Labor	The Fixed Cost	Software Update	Sub Total
	0	207.09	0	0	0	207.09
2012	1		$ 660.79	$ 1,006.92	$ 0.71	$ 1,668.42
2013	2		$ 680.62	$ 1,006.92	$ 0.71	$ 1,688.25
2014	3		$ 701.04	$ 1,006.92	$ 0.71	$ 1,708.67
2015	4		$ 722.07	$ 1,006.92	$ 0.71	$ 1,729.70
2016	5	$ 207.09	$ 743.73	$ 1,006.92	$ 0.71	$ 1,958.45
2017	6		$ 766.04	$ 1,006.92	$ 0.71	$ 1,773.67
2018	7		$ 789.02	$ 1,006.92	$ 0.71	$ 1,796.65
2019	8		$ 812.69	$ 1,006.92	$ 0.71	$ 1,820.32
2020	9		$ 837.07	$ 1,006.92	$ 0.71	$ 1,844.70
2021	10	$ 207.09	$ 862.18	$ 1,006.92	$ 0.71	$ 2,076.91
2022	11		$ 888.05	$ 1,006.92	$ 0.71	$ 1,895.68
2023	12		$ 914.69	$ 1,006.92	$ 0.71	$ 1,922.32
2024	13		$ 942.13	$ 1,006.92	$ 0.71	$ 1,949.76
2025	14		$ 970.40	$ 1,006.92	$ 0.71	$ 1,978.03
2026	15	$ 207.09	$ 999.51	$ 1,006.92	$ 0.71	$ 2,214.23
2027	16		$ 1,029.49	$ 1,006.92	$ 0.71	$ 2,037.12
2028	17		$ 1,060.38	$ 1,006.92	$ 0.71	$ 2,068.01
2029	18		$ 1,092.19	$ 1,006.92	$ 0.71	$ 2,099.82
2030	19		$ 1,124.96	$ 1,006.92	$ 0.71	$ 2,132.59
2031	20	$ 207.09	$ 1,158.70	$ 1,006.92	$ 0.71	$ 2,373.42
2032	21		$ 1,193.47	$ 1,006.92	$ 0.71	$ 2,201.10
2033	22		$ 1,229.27	$ 1,006.92	$ 0.71	$ 2,236.90
2034	23		$ 1,266.15	$ 1,006.92	$ 0.71	$ 2,273.78
2035	24		$ 1,304.13	$ 1,006.92	$ 0.71	$ 2,311.76
2036	25	$ 207.09	$ 1,343.26	$ 1,006.92	$ 0.71	$ 2,557.98
2037	26		$ 1,383.55	$ 1,006.92	$ 0.71	$ 2,391.18
2038	27		$ 1,425.06	$ 1,006.92	$ 0.71	$ 2,432.69
2039	28		$ 1,467.81	$ 1,006.92	$ 0.71	$ 2,475.44
2040	29		$ 1,511.85	$ 1,006.92	$ 0.71	$ 2,519.48
2041	30	$ 207.09	$ 1,557.20	$ 1,006.92	$ 0.71	$ 2,771.92
2042	31		$ 1,603.92	$ 1,006.92	$ 0.71	$ 2,611.55
2043	32		$ 1,652.04	$ 1,006.92	$ 0.71	$ 2,659.67
2044	33		$ 1,701.60	$ 1,006.92	$ 0.71	$ 2,709.23
2045	34		$ 1,752.64	$ 1,006.92	$ 0.71	$ 2,760.27
2046	35	$ 207.09	$ 1,805.22	$ 1,006.92	$ 0.71	$ 3,019.94
2047	36		$ 1,859.38	$ 1,006.92	$ 0.71	$ 2,867.01
2048	37		$ 1,915.16	$ 1,006.92	$ 0.71	$ 2,922.79
2049	38		$ 1,972.62	$ 1,006.92	$ 0.71	$ 2,980.25
2050	39		$ 2,031.80	$ 1,006.92	$ 0.71	$ 3,039.43

100

Year	Age					
2051	40	$ 207.09	$ 2,092.75	$ 1,006.92	$ 0.71	$ 3,307.47
2052	41		$ 2,155.53	$ 1,006.92	$ 0.71	$ 3,163.16
2053	42		$ 2,220.20	$ 1,006.92	$ 0.71	$ 3,227.83
2054	43		$ 2,286.80	$ 1,006.92	$ 0.71	$ 3,294.43
2055	44		$ 2,355.41	$ 1,006.92	$ 0.71	$ 3,363.04
2056	45	$ 207.09	$ 2,426.07	$ 1,006.92	$ 0.71	$ 3,640.79
2057	46		$ 2,498.85	$ 1,006.92	$ 0.71	$ 3,506.48
2058	47		$ 2,573.82	$ 1,006.92	$ 0.71	$ 3,581.45
2059	48		$ 2,651.03	$ 1,006.92	$ 0.71	$ 3,658.66
2060	49		$ 2,730.56	$ 1,006.92	$ 0.71	$ 3,738.19
2061	50		$ 2,812.48	$ 1,006.92	$ 0.71	$ 3,820.11
PV		$47,962.31 (S)			$8,825,064.86 (T)	
AW		$2,232.66 (S)			$410,808.54 (T)	